Lithos 318–319 (2018) 357–375

Contents lists available at ScienceDirect

Lithos

journal homepage: www.elsevier.com/locate/lithos

Petrogenesis of a ~900 Ma mafic sill from Xuzhou, North China: Implications for the genesis of Fe-Ti-rich rocks

Xiangdong Su [a,b], Peng Peng [a,b,*], Chong Wang [a,b], Fengbo Sun [a,b], Zhiyue Zhang [a,b], Xiaotong Zhou [a,b]

[a] State Key Laboratory of Lithospheric Evolution, Institute of Geology and Geophysics, Chinese Academy of Sciences, P.O. Box 9825, Beijing 100029, China
[b] University of Chinese Academy of Sciences, Beijing 100049, China

ARTICLE INFO

Article history:
Received 25 April 2018
Accepted 18 August 2018
Available online 24 August 2018

Keywords:
Fe-Ti-rich gabbro
Sill complex
Fractional crystallisation
Titanite
Neoproterozoic
North China Craton

ABSTRACT

The Niutishan sill, one of the ~900 Ma mafic sills in Xuzhou (Jiangsu province, North China), has a thickness of ~30 m. We have identified chemical parameters that define three differentiated interlayers from thirty-eight samples in a ~22 m profile. The sill reveals a succession consisting of an upper border zone of fine-grained dolerite (*UZ*), a middle zone of quartz-bearing gabbro (*MZ*), a coarse-grained apatite-enriched gabbro (*LZc*), a layer of Fe-Ti oxide-enriched gabbro (*LZb*) and a deeper medium-grained massive gabbro (*LZa*) at the bottom of the lower zone, capped by an uppermost chilled margin (*CM*) of plagioclase-clinopyroxene-porphyritic dolerite. Its significantly differentiated interlayers offer an opportunity to investigate the petrogenesis of high-Fe-Ti gabbro. The chilled margin composition suggests a highly evolved ferro-basaltic parental magma (whole-rock Mg#: 39, with ~2.9 wt% TiO_2 and ~14.2 wt% FeO_t), which likely represents a residual magma derived from a deep-seated magma chamber after significant removal of olivine. The internal compositional variation was controlled by fractional crystallisation with successive presence of plagioclase and Fe-poor clinopyroxene, followed by Fe-Ti oxides plus Fe-rich clinopyroxene, and finally apatite and albite-oligoclase. This sequence is consistent with the result of thermodynamic modelling of MELTS at a low H_2O content of ~0.2 wt% and in a temperature range from 1200 to 780 °C and at a pressure of 70 MPa. The saturation of clinopyroxene before Fe-Ti oxides in liquids is interpreted to imply low-fO_2 and water-unsaturated conditions, which led the residual magma to an Fe-Ti- enriched trend. After the saturation and mechanical settling of clinopyroxene primocrysts from the parental magma, large amounts of Fe-Ti oxides crystallised from the evolved Fe-Ti-rich melt. Further crystallisation and solidification of the crystal mush led to the formation of the major Fe-Ti oxide-rich layer and expelled interstitial melt upward to mix with the more evolved residual melts, leading to the saturation of apatite. Meanwhile, the residual melts gradually tended to Si enrichment, which matches the observed compositions (enriched incompatible elements) of naturally occurring quartz- gabbro in the *MZ*. As a result, viscosity would increase, trapping highly evolved melts and impeding liquid separation, as exhibited by the silicic mesostasis of graphic intergrowths of quartz and alkali feldspar, and occasionally calcite. This sill is also characterized by considerable amounts of titanite at the bottoms of the *UZ* and *LZ*, which was likely formed during the late evolutionary stages as products of reaction between the primary Ti-rich minerals and a late igneous fluid/melt at temperature near 584 °C. The F-rich and Cl-poor apatite ($X_F > 0.95$) and Ti-rich magnetite (7.2–9.7 wt% Ti) from Fe-Ti (P)-rich layers indicate a magmatic origin from high-temperature Fe-Ti-rich melts. It is thus concluded that the significantly differentiated Niutishan sill was formed by the combined processes of fractionation, accumulation and compaction under water-unsaturated and low-fO_2 conditions, which most likely occurred in an intra-continental rather than a subduction-related environment. Further synthetic analysis suggests conclusion that this magmatism may record a break-up event.

1. Introduction

Fe-Ti-rich basaltic/gabbroic rocks in volcanic units and layered intrusions (basic sills and dykes) remain one of the persistent petrogenetic puzzles. They are characterized by high FeO_t of >14 wt% and TiO_2 above 2 wt% (e.g., Deckart et al., 2005; Namur et al., 2010; Prytulak and Elliott, 2007), and commonly contain varying amounts of Fe-Ti oxides with apatite. They are conducive to forming Ni-PGE (platinum group elements) sulphide and Fe-Ti-V-Cr oxide deposits (e.g., Dymek and Owens, 2001; Hanski and Smolkin, 1995; Jakobsen et al., 2011; Zhou et al., 2005).

Typical mantle-derived basalts have FeO_t contents of 7–10 wt% and TiO_2 <1 wt% (e.g., Danyushevsky et al., 2003; Falloon et al., 1999).

* Corresponding author at: State Key Laboratory of Lithospheric Evolution, Institute of Geology and Geophysics, Chinese Academy of Sciences, P.O. Box 9825, Beijing 100029, China.
E-mail address: pengpengwj@mail.iggcas.ac.cn (P. Peng).

https://doi.org/10.1016/j.lithos.2018.08.023
0024-4937/

Further, FeO_t is ≤14 wt% and TiO_2 ≤2 wt% in some high-MgO picrites from oceanic (e.g., Hawaii, Iceland, St Helena) and continental intraplates (e.g., Emeishan, Deccan, Pechenga, West Greenland and Karoo). Therefore, the source properties and petrogenesis of Fe-Ti-rich magmas have been hotly debated: (1) Fe-Ti rich residual melt can be produced by the fractional crystallisation of mafic magmas under low-fO_2 and water-unsaturated conditions (e.g., Charlier et al., 2008; Namur et al., 2012; Owens and Dymek, 2001); (2) magma immiscibility is another mechanism to produce high-Fe-Ti rocks (e.g., Charlier et al., 2011; Charlier and Grove, 2012; Philpotts, 1982; Veksler et al., 2007; Zhou et al., 2005); (3) some eruptive Fe-Ti-rich lavas could have originated directly from a mantle source without significant differentiation (e.g., Gibson et al., 2000), and the Fe-Ti-rich mantle source was attributed to crust-mantle interaction including, for example, contamination of high-Ti eclogite or recycled oceanic crust (Prytulak and Elliott, 2007; Sobolev et al., 2007) or hybridization with high-Ti mafic-potassium melts from the continental lithospheric mantle (Gibson et al., 1996). There is no current consensus as to which one of these mechanisms prevails, or under what conditions each mechanism plays an important role. Therefore, research on Fe-Ti-rich mafic-ultramafic layered intrusions has great bearing on validating many assumptions about liquid trends, calibrating the evolution of tholeiitic basalts and the petrogenesis of evolved Fe-Ti-rich rocks (e.g., Jakobsen et al., 2005; Namur et al., 2010), and monitoring feasible crustal conditions and broad tectonic backgrounds in forming Fe-Ti-rich magmas.

Recently, many ~900 Ma rocks have been identified in the North China craton (NCC) (Peng et al., 2011a, 2011b; Wang et al., 2012; Zhang et al., 2016). Most of these rocks are enriched in Fe and Ti, which provides a new material to study high Fe-Ti rocks (Table 1), as exemplified by the Chulan sill complex in the southeast NCC. Previous studies mainly focused on the geochronology and whole-rock chemistry of the relevant intrusions; and little is known about their petrogenesis and magmatic evolution. Among them, the Niutishan sill in Xuzhou (Jiangsu Province) is being mined, and its typical interior layering inside with an Fe-Ti-rich layer provides a chance to further investigate the petrogenesis of high-Fe-Ti rocks. Here, we report whole-rock and mineral data from a specific profile of the sill to investigate the differentiation responsible for forming the Fe-Ti-rich rocks.

2. Geological setting

There is a series of ~ 900 Ma mafic intrusions, e.g., the ~900 Ma Sariwon sills in Pyongnam basin (North Korea) (Peng et al., 2011b), the 890–920 Ma Dalian sills in the Lv-Da basin (Liaodong Peninsula) in the eastern NCC (Zhang et al., 2016), the 925 Ma Dashigou dyke swarm in the central NCC (Peng et al., 2011a) (Fig. 1a) and the 890–920 Ma Chulan sills in the Xuzhou-Huaibei area (Peng et al., 2011b; Wang et al., 2012) (Fig. 1b). Among them, the Chulan gabbroic sills in the dolomite-dominated Huaibei Group cover an area of approximately 45 (N-S) × 60 (*E*-W) km^2, with thicknesses varying from 15 to 200 m.

The Huaibei Group, composed of conglomerate, quartz sandstone, marlite and shale with limestone interlayers ~4000 m thick in total, is in unconformable contact with both the Archaean crystalline basement and the overlying Cambrian limestone. The Huaibei Group can be divided into thirteen formations. The Chulan sill complex conformably intruded into the host limestone of the Shijia Fm., Wangshan Fm., Jiudingshan Fm., Niyuan Fm. and Zhaowei Fm. The ages of these sills range from 890 to 920 Ma (Peng et al., 2011b; Wang et al., 2012). These basic sills are suggested to show an affinity with N-MORB to E-MORB (Wang et al., 2012) or to have been generated from a mantle plume sourced in the asthenosphere (Peng et al., 2011a).

Near Niutishan Village, ~46 km from Xuzhou, there is one of these sills, which has a thickness of ~30 m and length of >6 km. Rocks near the edge of the intrusion dip south-east at 17°, giving an overall shape

Table 1
Petrography and mineral assemblage of Fe-Ti rich dykes and sills in the NCC.

Sample no.	locality	SiO_2 (wt%)	FeO_t (wt%)	TiO_2 (wt%)	Mg#	Texture	Mineral assemblage	Age(Ma)	Methods	Reference
03JH011 (Ave. Group 1)	Liaodong penisula	47.87	14.77	2.50	45.3	Ophitic texture	Cpx + Pl + Mt. + Ilm +Ap ± Tit±Kf	904 ± 15	Zircon, SHRIMP	Yang et al. (2007)
11197-1 to 11227-1		48.64	15.46	3.08	36.4	Ophitic texture	Cpx + Pl ± Hb ± Mt. ±Ilm ± Kf ± Bi	890–920	Zircon and Baddeleyite, SIMS	Zhang et al. (2016)
02SX103	Dashigou H–engshan Mts.	52.63	15.70	3.18	36.0	Ophitic texture	Cpx + Pl + Ilm ± Ol	924.0 ± 3.8	Baddeleyite, ID-TIMS	Peng et al. (2011a)
08LC20, 03LC04, 05LC06 (Ave.)	Liangcheng, Shanxi province	50.77	16.20	3.04	36.3	Ophitic texture		921 ± 2.1		
05ZQ09	Zuoquan, Taihang Mts.	48.69	15.40	4.39	40.0	Ophitic texture				
XZ1-1, 3, 5 XZ3-2, 4 XZ5-3, 6, 7	Xuzhou, Jiangsu province	47.36	14.29	2.77	40.0	Ophitic texture	Cpx + Pl + Qz + Hb +Mt. + Bi	887–933	Zircon, Q-ICP-MS	Wang et al. (2012)
NS01-03 (Ave.)		48.82	14.28	2.89	38.7	porphyritic texture	Phe: Cpx + Pl Gro:Cpx + Pl + Fe -Ti oxides+Qz			This study
NS32-34 (Ave.)		45.75	18.72	3.93	30.0	Medium-gabbro	Cpx + Pl + Fe-Ti oxides+Py + Ttn+ Ap ± Hb			
NS34-40 (Ave.)		49.36	12.86	2.56	41.5	texture				

Cpx, clinopyroxene; Pl, plagioclase; Hb, hornblende; Mt., magnetite; Ilm, ilmenite; Ap, apatite; Ttn, titanite; Py, pyrite; Bi, biotite; Phe, phenocrystal; Gro, groundmass.
Mg# = molar value of 100*MgO/(FeO_t + MgO)

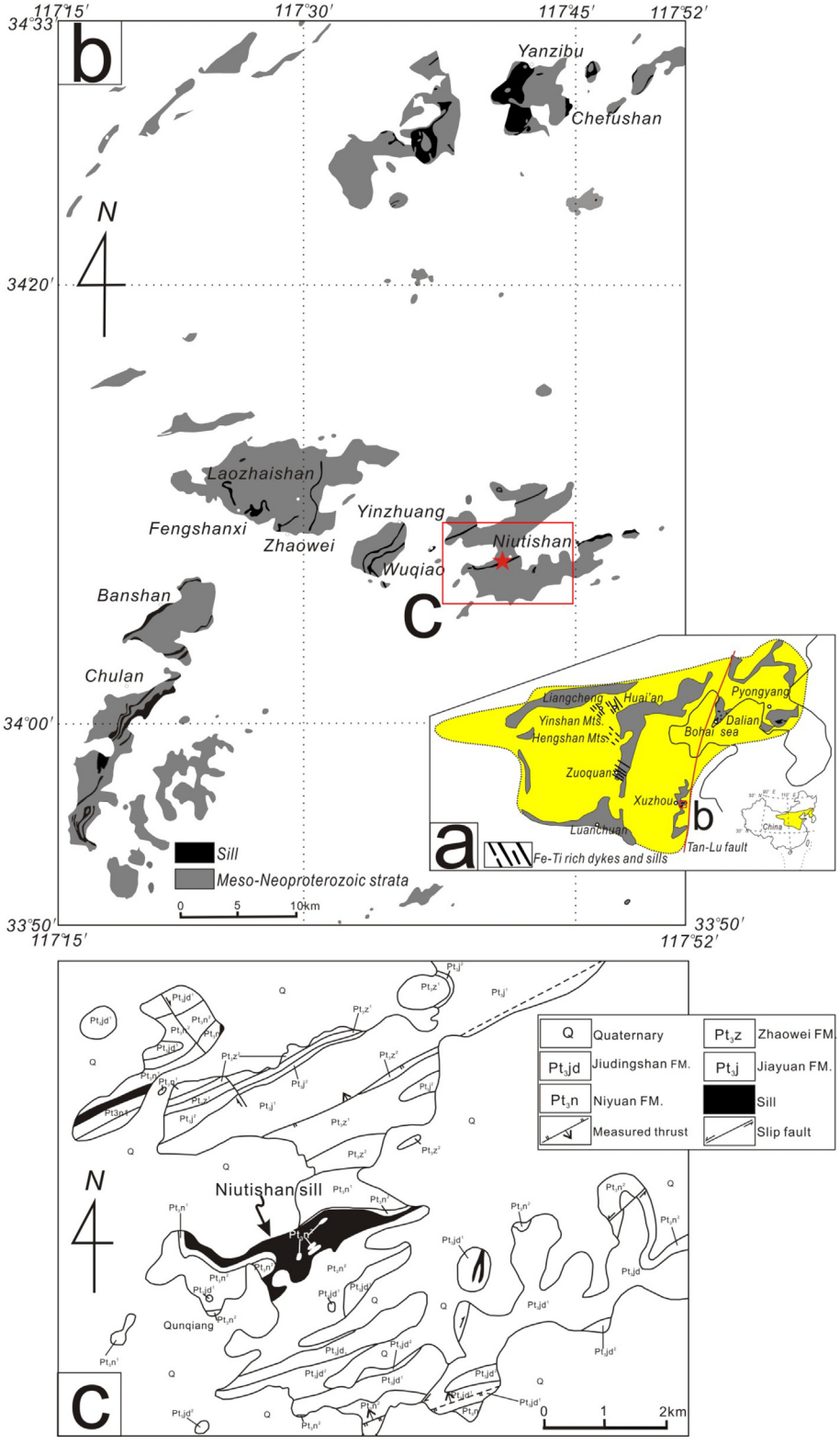

Fig. 1. (a) Sketched map showing the distribution of Neoproterozoic mafic dykes and sills (~900 Ma) with related associations in NCC (Modified after Peng et al., 2011a and Zhang et al., 2016). (b) The distribution of Chulan sill complex in Xuhuai area at southeastern NCC, all of them intruded into the Neoproterozoic strata of Huaibei Group. The red star shows the Niutishan sill. (c) The planar graph of the Niutishan sill and related association in this area.

like that of a 'shrimp' (Fig. 1c). Most of its volume is hidden beneath the dolomite of the Niyuan Fm. A thin border of very fine-grained dolerite is observed in the contact zone between the intrusion and the country rocks, which is traditionally interpreted as a chilled margin, representing magma that was rapidly cooled against the cold country rocks.

3. Sampling and analytical methods

3.1. Sampling

A total of 38 samples were collected systematically with a constant spacing of ~0.5 m from the top to the bottom of the Niutishan sill. The true stratigraphic position and the distance between samples were corrected based on the average local dip (17° SE). The real outcrop thickness of this sill is ~22 m, and the top surface was set to '0 m'. The erosion surface of sample was carefully removed. All analytical procedures were accomplished at the Institute of Geology and Geophysics, Chinese Academy of Sciences (IGGCAS).

3.2. Whole-rock analysis

Sample powders, ~0.5 g for each, were fused into a glass bead with ~5.0 g of lithium tetraborate. Major elements were measured using a PANalytical AXIOS Minerals instrument, and ferrous iron was measured by titration (Table 2 and Supplementary Table 1). The uncertainties for major elements were < 1.0 wt%. The precision was better than 0.2 wt% in the analytical range. The loss-on-ignition (LOI) was determined by the weight loss for a powdered sample after 2 h heating at 1000 °C and 30 min cooling to ambient temperature. Two reference materials GSR1 and GSR3 were measured to evaluate the chemical preparation procedure and the condition of the instrument. GSR1 and GSR3 data are listed in Supplementary Table 1, and are consistent with the reference values.

Whole-rock trace element analyses were determined using an ELEMENT instrument after HNO_3 + HF digestion of approximately 40 mg of sample powder in a Teflon vessel, with accuracy and reproducibility monitored using Chinese national standard samples GSR1 and GSR3. GSR1 and GSR3 data are listed in Supplementary Table 1 and are consistent with the reference values. Both precision and accuracy are better than 5% for most of the trace elements (Table 2 and Supplementary Table 1).

3.3. Electron microprobe mapping and analysis

Thin and polished sections of the gabbroic rocks that were coated with carbon were made for the analysis of major elements and backscattered electron images. Major element compositions of plagioclase, clinopyroxene, apatite and ilmenite were obtained by a JEOL JXA 8100 instrument (an electron microprobe analysis). Quantitative analyses were performed using wavelength-dispersive spectrometers (WDS) with an acceleration voltage of 15 kV, a beam current of 20 nA, and a defocused beam size of 5 μm. Major element compositions of titanite,

Table 2
Selected representative major (wt%) and trace (ppm) elements data in the Niutishan sill.

Sample:	*CM*	*UZ*		*MZ*				*LZc*	*LZb*	*LZa*
	NS-01	NS-04	NS-09	NS-11	NS-15	NS-21	NS-28	NS-31	NS-32	NS-38
Depth(m)	−0.02	−0.81	−3.08	−4.06	−6	−9.39	−16.18	−17.21	−17.69	−20.87
SiO_2	*48.95*	*48.81*	*48.51*	*53.33*	*53.81*	*53.38*	*55.17*	*52.95*	*48.41*	*48.17*
TiO_2	*2.90*	*2.89*	*3.28*	*2.35*	*2.11*	*2.29*	*2.03*	*2.26*	*3.89*	*2.94*
Al_2O_3	*12.71*	*12.66*	*12.14*	*12.12*	*12.17*	*12.20*	*11.92*	*12.22*	*11.60*	*12.88*
TFe_2O_3	*15.62*	*15.85*	*16.88*	*15.78*	*15.84*	*16.53*	*15.42*	*17.06*	*18.33*	*15.90*
MnO	*0.24*	*0.23*	*0.27*	*0.22*	*0.23*	*0.25*	*0.26*	*0.28*	*0.27*	*0.23*
MgO	*5.04*	*5.01*	*4.71*	*2.25*	*2.12*	*2.40*	*1.83*	*1.97*	*3.98*	*5.15*
CaO	*8.91*	*8.79*	*7.90*	*5.94*	*5.91*	*5.91*	*6.06*	*6.03*	*7.86*	*9.30*
Na_2O	*3.40*	*3.15*	*3.09*	*3.68*	*3.60*	*3.48*	*3.75*	*3.51*	*3.14*	*2.63*
K_2O	*0.51*	*0.70*	*0.94*	*1.04*	*0.93*	*1.06*	*0.82*	*0.95*	*0.64*	*1.11*
P_2O_5	*0.30*	*0.30*	*0.35*	*0.60*	*0.66*	*0.60*	*0.71*	*0.85*	*0.38*	*0.25*
LOI	*2.02*	*1.84*	*2.32*	*2.80*	*2.24*	*2.12*	*1.78*	*2.08*	*1.98*	*1.66*
Total	*100.60*	*100.23*	*100.38*	*100.10*	*99.62*	*100.22*	*99.75*	*100.15*	*100.48*	*100.23*
FeO	*11.16*	*12.09*	*13.63*	*10.29*	*11.35*	*11.90*	*11.20*	*11.72*	*13.33*	*10.81*
Mg#	*38.80*	*38.30*	*35.39*	*21.90*	*20.82*	*22.20*	*18.91*	*18.50*	*29.91*	*38.90*
Th	2.95	2.80	3.32	6.49	7.08	6.09	7.29	6.47	3.94	2.29
U	0.61	0.64	0.71	1.43	1.49	1.21	1.53	1.31	0.87	0.48
Nb	15.54	15.22	18.32	30.40	31.79	27.14	33.56	31.53	22.59	13.55
Ta	1.07	1.06	1.26	2.10	2.26	1.82	2.32	2.13	1.62	0.89
Sr	245.07	251.48	219.72	155.48	169.23	163.28	181.77	198.43	183.66	220.44
Zr	183.75	177.04	209.32	373.46	389.40	351.27	415.69	355.26	255.94	147.04
Hf	5.19	5.18	5.92	10.73	11.74	9.81	11.97	10.10	7.40	4.15
Y	35.94	35.94	42.40	68.18	73.34	65.91	78.32	70.63	48.96	32.07
V	406.44	392.72	482.74	89.87	58.60	86.37	30.59	39.07	397.74	514.85
Cr	61.95	63.54	48.61	76.49	51.79	51.47	54.32	74.81	26.26	106.86
Co	43.26	43.95	44.57	26.80	23.58	27.08	24.76	26.37	50.63	42.51
Ni	38.27	34.87	30.29	1.71	1.41	5.84	0.68	2.04	1.98	46.87
La	18.92	18.72	22.15	39.04	43.71	38.67	44.25	39.47	24.62	16.05
Ce	41.96	41.57	49.37	86.26	97.39	83.55	99.18	89.50	57.08	35.14
Pr	6.09	6.00	7.19	12.58	14.09	12.12	14.44	13.08	8.19	5.04
Nd	26.31	26.56	31.61	54.71	60.11	52.54	64.35	58.25	35.85	21.96
Sm	6.82	7.00	8.10	13.68	14.88	13.08	15.90	15.11	9.63	5.87
Eu	2.23	2.27	2.64	4.23	4.46	3.81	4.43	4.08	2.97	1.93
Gd	7.25	7.25	8.88	14.58	15.70	13.75	16.60	15.25	9.87	6.24
Tb	1.20	1.20	1.47	2.39	2.75	2.31	2.81	2.63	1.67	1.07
Dy	7.42	7.63	8.96	14.64	15.99	13.53	16.80	15.52	10.60	6.49
Ho	1.50	1.52	1.84	3.03	3.21	2.73	3.61	3.22	2.24	1.34
Er	4.09	4.03	4.85	7.94	8.71	7.49	9.27	8.25	5.81	3.50
Tm	0.59	0.57	0.69	1.12	1.23	1.03	1.27	1.15	0.82	0.50
Yb	3.68	3.59	4.23	6.83	7.52	6.51	8.03	7.18	5.15	3.17
Lu	0.55	0.55	0.64	1.02	1.15	0.98	1.23	1.11	0.78	0.48

Mg# = molar value of 100*MgO/ (FeO_t + MgO); FeO_t = FeO + 0.8998*Fe_2O_3; Fe_2O_3=TFe_2O_3-1.1*FeO; ferrous iron is measured by titration. *CM*, the chilled margin; *UZ*, the upper zone; *MZ*, the middle zone; *LZa*, the massive gabbro in the bottom of the lower zone; *LZb*, the Fe-Ti-rich gabbro in the lower zone; *LZc*, the apatite-rich gabbro in the uppermost of the lower zone.

titano-magnetite and ilmenite lamellae were measured by CAMECA SX Five FE instrument (an electron probe micro-analyser). Quantitative analyses were performed using wavelength-dispersive spectrometers (WDS) with an acceleration voltage of 15 kV, a beam current of 30 nA, and a focused beam size (0 μm). The peak counting time was 10–20 s for all elements, and the background counting time was 10 s on the high- and low-energy background positions. All data were corrected online using a modified ZAF (atomic number, absorption, fluorescence) correction procedure. The detection limits were in the range of 0.008–0.02 wt% (1σ). The accuracy was generally <1 wt% for oxide contents >5 wt% (Supplementary Tables 2-7).

3.4. Fe-Ti two-oxide geothermometer and oxygen barometer

There are a few preserved coexisting titano-magnetite and ilmenite grains in the thin sections, due to the exsolved mature of ilmenite in oxide pairs. The titano-magnetite and nearly coeval thick ilmenite lamellae led to our adoption of a revised Fe-Ti two-oxide geothermometer and oxygen barometer. Temperature and oxygen fugacity were calculated using the online MELTS software (http://melts.ofm-research.org). The calculations were performed using the model of Ghiorso and Evans (2008). The results include the Fe-Ti exchange temperature, fO_2 (relative to NNO) and $aTiO_2$ (liquid, relative to rutile saturation). NNO refers to the nickel-nickel oxide oxygen buffer, as calculated from O'Neill and Pownceby (1993) using the pressure correction suggested by Frost (1991) with an assumed pressure of 200 MPa. The liquid activity of TiO_2 is calculated by evaluating the equilibrium reaction: 2 $FeTiO_3$ (component in ilmenite) = Fe_2TiO_4 (component in magnetite) + TiO_2 (liquid component). The results are shown in Supplementary Table 5.

3.5. Titanite LA-ICP-MS trace element analysis and Zr-in-titanite thermometry

Titanite trace elements were analysed by using an LA-ICP-MS system composed of an Agilent 7500a ICP-MS coupled with a Resonetic RESOLution M–50 ArF–Excimer laser source (λ = 193 nm). The pulse width was 15 ns. The laser energy was 98 mJ, with a repetition rate of 8 Hz, spot sizes of 44 μm and 60 μm in diameter and a total of 45 s ablation time. Helium was used as the carrier gas to enhance the transport efficiency of the ablated material. Trace concentrations were calibrated by using ^{29}Si as an internal standard and NIST SRM 610 as the reference standard. The element concentrations were measured using the GLITTER 4.0 software (Griffin et al., 2008) for elemental fraction correction. The data after calibration (1σ) are shown in Supplementary Table 8.

A powerful tool to calculate the crystallisation temperature is the Zr-in-titanite thermometer. Because the closure temperature of titanite can be as high as 800 °C (Kohn, 2017), and some titanite core Zr abundances yield Zr-in-titanite temperatures >850 °C (Garber et al., 2017). Zr-in-titanite temperatures were calculated for a quartz- and titanite-bearing, rutile-absent sample (NS-08) using the Hayden et al. (2008) calibration:

$$T(^{\circ}C) = \frac{[7708 + 960P(GPa)]}{[10.52 - \log(a_{TiO_2}) - \log(a_{SiO_2}) - \log(ppm\ Zr, titanite)]} - 273$$

where a_{SiO_2}=1 and $a_{TiO_2} = 0.22 \pm 0.01$ (2σ, $n = 6$); pressure is based on the total Neoproterozoic sedimentary strata thickness overlaying the Niutishan sill, corresponding to the lithostatic pressure at a depth of 2.2 km. Reported temperatures in Supplementary Table 8 are the weighted average of multiple spots from a single sample.

4. Results

4.1. Overview of the lithological stratigraphy and mineral composition

The most remarkable features of the Niutishan sill are the presence of one apatite-rich and one Fe-Ti oxide-rich interlayers. The petrographic boundaries are clear in the field. Most of the series is equi- to hetero-granular and fine- to medium-grained (0.5–5 mm). The original igneous texture is well preserved (Fig. 2). Plagioclase and clinopyroxene are the most abundant minerals, whereas inverted titano-magnetite, ilmenite, titanite, apatite, chlorite, quartz, alkali feldspar and Fe-sulphides are subordinate (Fig. 3). In terms of petrography and whole-rock chemistry, we suggest that this sill is subdivided into four units: the chilled margin (*CM*), the upper zone (*UZ*), the middle zone (*MZ*) and the lower zone (*LZ*).

4.1.1. The chilled margin (CM)

The *CM* (0 to −0.3 m) zone is compositionally uniform and contains clinopyroxene and plagioclase phenocrysts (Fig. 2a). The size of clinopyroxene phenocrysts can reach 1 mm. The Mg-number and En of Cpx phenocrysts are approximately 0.74–0.75 and 45.6–46.7, respectively, while the values for the matrix Cpx are 0.68–0.70 and 38.0–42.8, respectively.

4.1.2. The upper zone (UZ)

The *UZ* (−0.3 to −3.5 m) is made up of fine-grained dolerite (Fig. 2b), which is composed of euhedral clinopyroxene (45–55 vol%) and plagioclase (15–24 vol%), Fe-Ti oxides, and minor titanite (5–8 vol%) and quartz (1–5 vol%) (Fig. 2). The grains sizes of plagioclase and clinopyroxene mostly range from 0.5 to 1.5 mm, with a few plagioclase grains reaching 4 mm. This fine-grained dolerite may represent rapidly cooled magma nearing in situ crystallisation. Some small rhombohedral to prismatic euhedral titanite grains (~0.1–0.5 mm) from the base of the *UZ* (Fig. 4a) do not show any sector or oscillatory zoning while exhibit an irregular intergrowth relationship with ilmenite. The plagioclase An (45 to 60) and Cpx Mg-number (0.63–0.71) are slightly lower than those in the *MZ*.

4.1.3. The middle zone (MZ)

The *MZ* (−4 to −17.2 m) comprises quartz gabbro of tabular plagioclase (30–55 vol%) with interstitial clinopyroxene (12–20 vol%), quartz (10–15 vol%), minor Fe-Ti oxides (4–8 vol%) and rare apatite (0–1 vol%) (Fig. 3a). Plagioclase occurs as large grains (2–5.5 mm), which randomly form a triangular grillwork that is mostly filled with a silicic mesostasis of graphic intergrowths of quartz and alkali feldspar (Fig. 2d). Clinopyroxene appears fine-grained (0.5–3 mm) euhedral to subhedral and granular, but some grains have regressed to amphibole. The interstitial alkali feldspar and quartz (3–12 vol%) (Fig. 2d) have features of a mineral assemblage and indicate a residual trapped melt, which is merely a present phase in the *UZ* and underlying *LZ*. The acicular ilmenite appears to occur at the base of the *MZ*, as does the comb-like ilmenite intergrowing with chlorite, albite, quartz and zircon (Fig. 4i). Some thin titanite rims (<2 μm) are observed around ilmenite (Fig. 4b). Irregular pyrite is a ubiquitous phase in the samples (Fig. 2b). The An number (of plagioclase) shows little variation between −17 and − 8 m (from An_{50} to An_{30}) but rapidly decreases to An_{2-16} between −7 and − 4 m. This En and Mg-number increase up-section from the base of the *MZ* to the *UZ* but show odd minimum values between −16.5 and − 13 m (Fig. 3b).

4.1.4. The lower zone (LZ)

The *LZ* is made up of one apatite-rich layer (−16.5 to −17.5 m, *LZc*) and an underlying Fe-Ti oxide-rich layer (−17.5 to −18.5 m, *LZb*) as well as medium-grained massive gabbro at the bottom of the lower zone (−17.5 to −22 m, *LZa*). There is no clear margin between the *MZ* and *LZ*, nor between the sub-layers. Apatite and Fe-Ti oxide phases

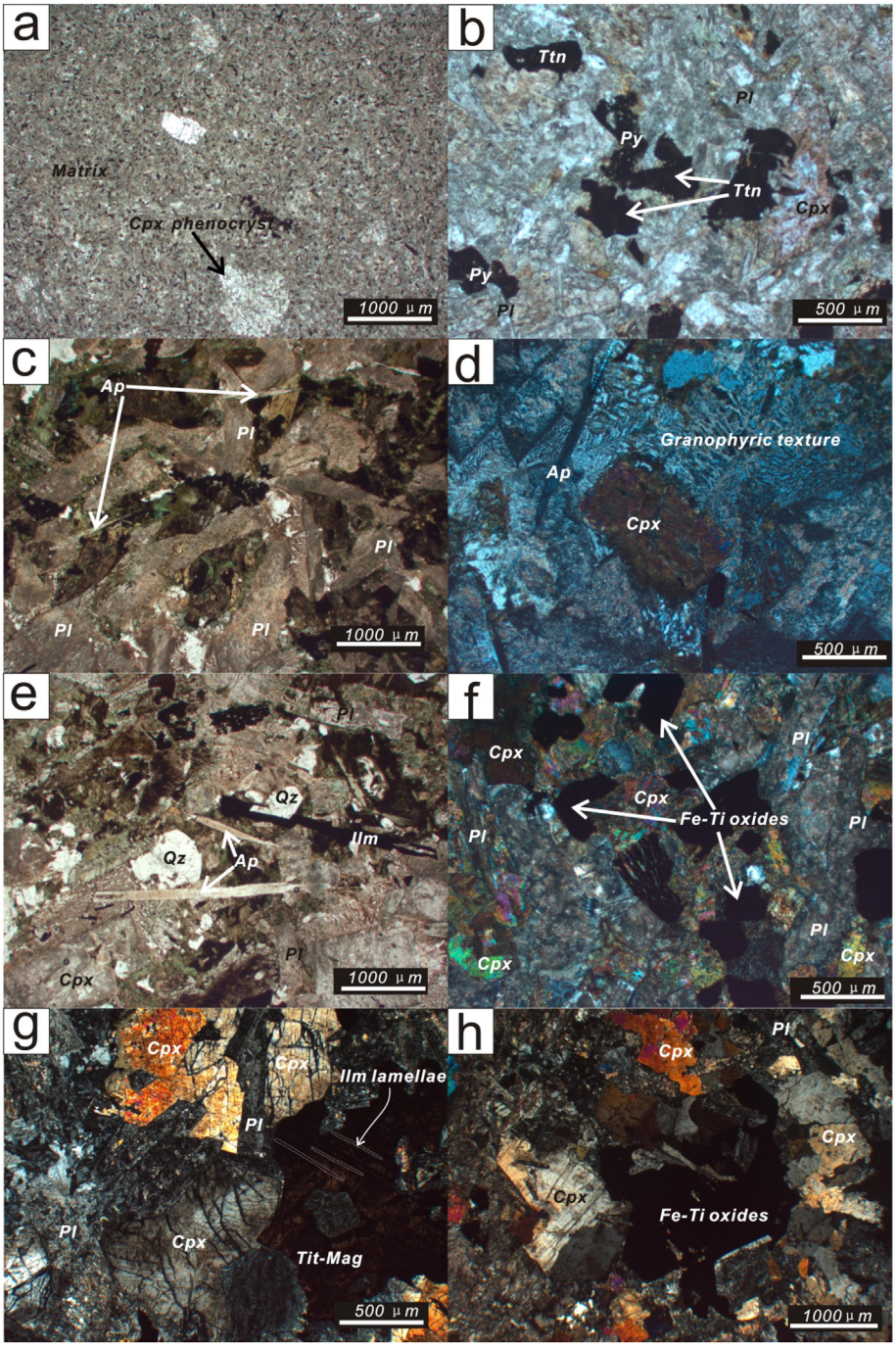

Fig. 2. Photomicrographs showing mineral textural in the Niutishan sill. (a) Chilled margin with euhedral grains of clinopyroxene phenocrysts in porphyritic texture. The matrix is made up of plagiocalse, clinopyroxene and Fe-Ti oxieds (Sample NS-01; *CM*). (b) Dolerite showing millimeter-scale euhedral clinopyroxene, plagioclase, Fe-Ti oxides and titanite in fine grained texture (Sample NS-08; *UZ*). (c) Triangular plagioclase lattice was filled with chlorites and quartz (Sample NS-12, *MZ*). (d) Granophyric texture showed in Quartz-gabbro is made up of quartz and kf-feldspar (Sample NS-27, *MZ*). (e) Gabbro from the apatite-rich layer with many needle-like or hexagonal-grain shape of apatite (Sample NS-31, *LZc*). (f) Gabbro with amount of Fe-Ti oxides, granular clinopyroxene and tabular plagioclase (Sample NS-32, *LZb*). (g) Gabbro with euhedral clinopyroxene, plgioclase and subhedral titano-magnetite (Sample NS-40, *LZa*); the ilmenite lamellae within large titano-magneitte should be noted. (h) Gabbro with medium clinopyroxene and plagioclase grains. Some earlier clinopyroxene and plagioclase oikocrysts enclosed by the poikilitic Fe-Ti oxides should be noted (Sample NS-37, *LZa*). Pl, plagiocalse; Cpx, clinopyroxene; Ap, apatite; Ttn, titanite; Py, pyrite.

can reach ~3 vol% and 20 vol%, respectively. Equant apatite generally has a hexagonal shape (35–350 μm in diameter), while acicular apatite can grow to a large size (0.2–2.3 mm). Samples from *LZa* (Fig. 2g, h) are compositionally uniform and consist of massive gabbro with tabular plagioclase (30–50 vol%) and euhedral clinopyroxene (30–45 vol%). The silica-rich mesostases are very rare. Titano-magnetite (5–10 vol%) and apatite (0–2 vol%) are subordinate phases. The sizes of tabular euhedral to subhedral plagioclase grains are 0.1–2 mm but show little alteration. Clinopyroxene occurs as euhedral to subhedral prismatic grains. Poikilitic textures are locally prominent such that some embayed clinopyroxene and plagioclase grains are enclosed by Fe-Ti oxide oikocrysts (Fig. 2g, h), suggesting that clinopyroxene and plagioclase were saturated before Fe-Ti oxides in liquids. Titano-magnetite commonly contains ilmenite lamellae (Fig. 2g). Two types of ilmenite lamellae are identified: the first larger sandwich-type lamellae (3–7 μm) and the second finer-grained, trellis-type lamellae (≤1 μm) (Fig. 4k). Titano-magnetite and ilmenite lamellae are significantly replaced by tiny-spot titanite (≤5 μm, Fig. 4c, d), and some of

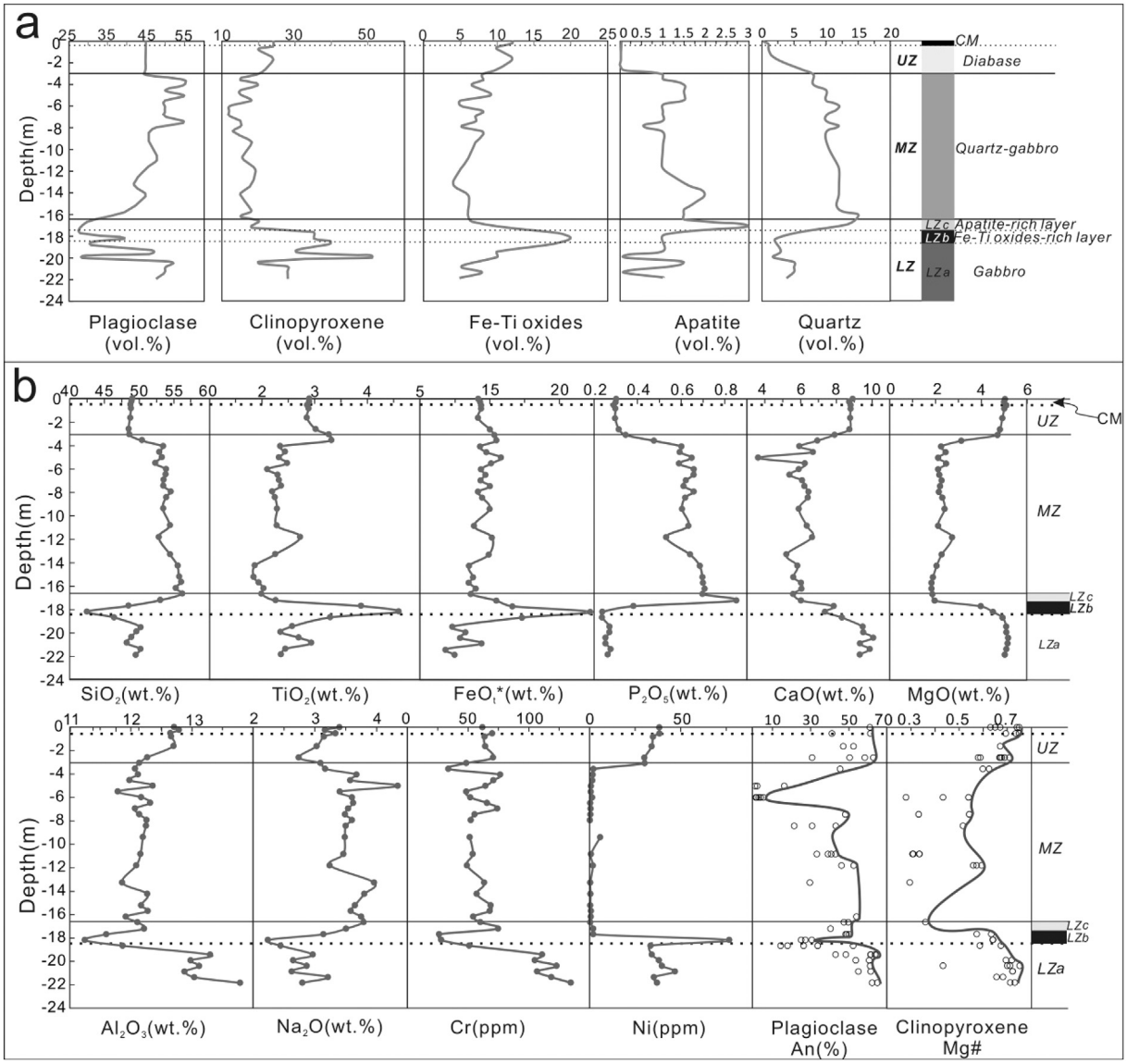

Fig. 3. (a)Mineral proportion of plagioclase, clinopyroxene, Fe-Ti oxides, apatite, and quartz and subdivision of the Niutishan sill. Solid line represents the boundaries of zones. (b) Compositional variation of whole-rocks and plagiocalse, clinopyroxene in the cross section. Solid lines represent boundaries of zones.

them are totally replaced by titanite (Fig. 4e, f). Clinopyroxene that coexists with titano-magnetite is generally free from significant alteration such as chloritization and montmorillonitization. The euhedral ilmenite mostly coexists with titano-magnetite while some of the titano-magnetite is occasionally surrounded by secondary ilmenite rims (Fig. 4c).

Both clinopyroxene and plagioclase show a compositional evolution in that the An, Cpx Mg-number and En decrease continuously from $An_{50–62}$ to An_{27}, 0.67 to 0.57 and En_{38} to En_{30}, respectively, from *LZa* upward to *LZc* (Supplementary Tables 2-3). Clinopyroxene is normally zoned with compositional differences from core to rim (by EPMA, Fig. 5a, b). The X_F (X_F = mole [F/(F + Cl)] of apatite in *LZc* is >0.95 (Supplementary Table 4). The titano-magnetite is characterized by no significant variations in SiO_2 (0.06–0.1 wt%) and CaO (0.07–0.23 wt%), depletion in relatively immobile elements such as Cr (100–300 ppm), and enrichment in Ti (7.2–9.7 wt%) with extremely low Ni/Cr values. Distinct ilmenite grains in different layers show similar ranges of MgO (0–0.24 wt%) and MnO (1.7–2.4 wt%). The $MnTiO_3$ and $FeTiO_3$ in ilmenite (X_{pyr} and X_{ilm}) are 3.27–4.99% and 84.59–96.09%, respectively (Supplementary Table 6).

4.2. Whole-rock geochemical composition

4.2.1. Major elements

The whole-rock composition of gabbro in *LZa* is rich in MgO (5.0–5.2 wt%) and CaO (9.3–10.1 wt%) but depleted in SiO_2 (48.2–50.1 wt%). Al_2O_3 contents range from 12.9 to 13.8 wt%. FeO_t and TiO_2 range from 11.9 to 14.4 wt% and from 2.3 to 2.9 wt%, respectively. There are prominent increases in FeO_t and TiO_2 upward to the *LZb* of 16.6–22.2 wt% FeO_t and 3.3–4.6 wt% TiO_2. P_2O_5 is highest in *LZc* (P-rich horizons) and decreases upward though the body (Fig. 3b). From *LZc* upward to the *MZ*, SiO_2 contents range from 52.2 to 56.1 wt% and CaO contents from 3.7 to 6.7 wt%. Na_2O and K_2O range from 3.2 to 4.0 wt% and 0.6 to 0.7 wt%, respectively. Al_2O_3 contents range from 11.9 to 12.3 wt%. Obviously, SiO_2, Na_2O and K_2O significant increase but MgO, CaO, FeO_t, TiO_2 and Al_2O_3 decrease from the *LZ* upward to the *MZ* (Fig. 3b). There is a secondary reversal in the sill where MgO (3.1–5.1 wt%), CaO (6.9–8.9 wt%) and TiO_2 (2.9–3.3 wt%) increase and the SiO_2 (48.4–48.9 wt %), P_2O_5 (0.29–0.35 wt%) and total alkali contents decrease from the *MZ* upward to the *UZ* (Fig. 3b). From *LZa* to the overlying *LZb*, the significantly increasing accumulation phase of Fe-Ti oxides is underlined by

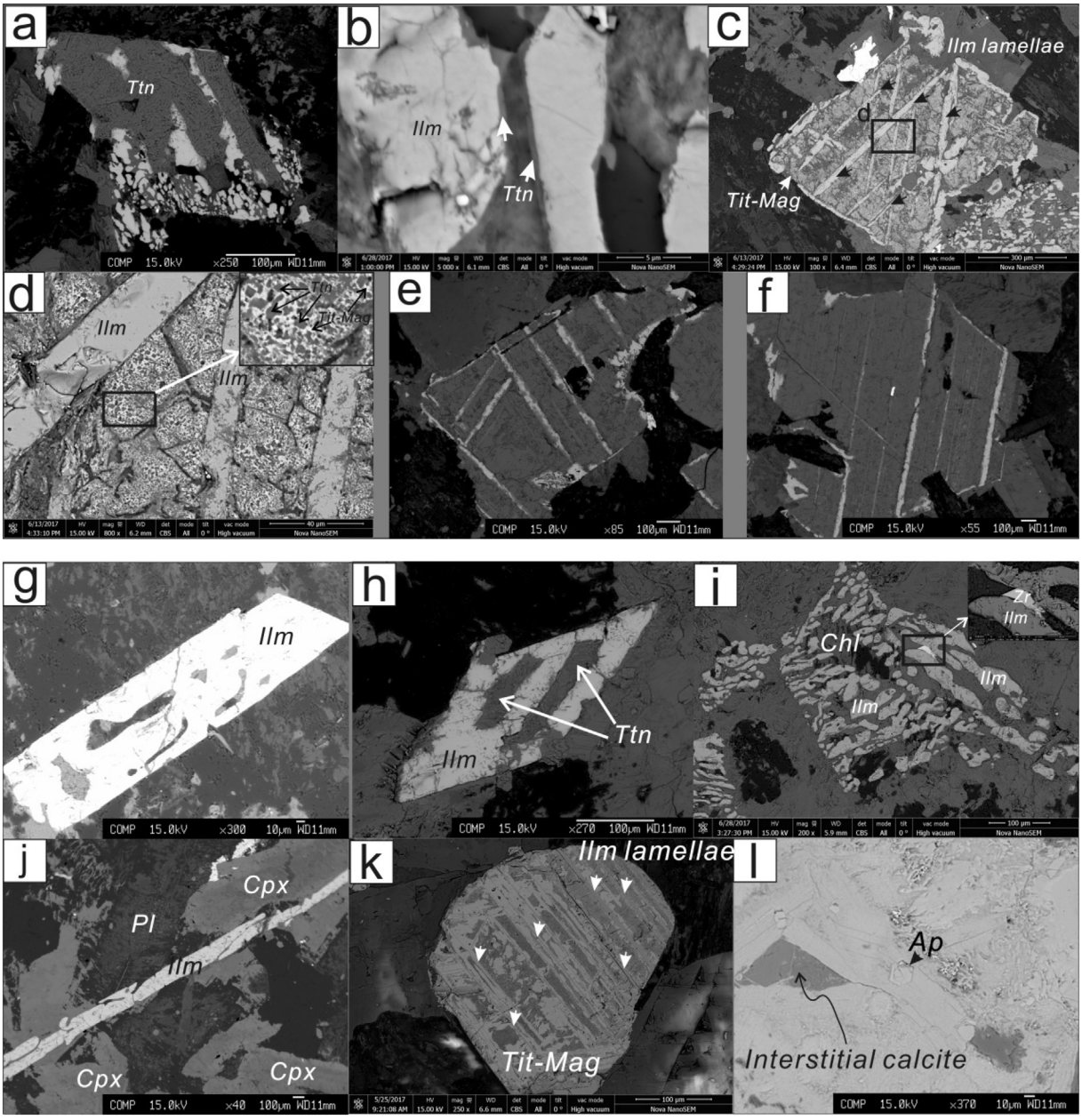

Fig. 4. The BSE of three forms titanite and six forms of ilmenite. (a) Euhedral-rhombohedral titanite grains with small size (~0.1–0.5 mm) partial replace limenite (Sample NS-08, *UZ*). (b) The photomicrograph showing secondary thin titanite rim (<1 μm) around ilmenite (sample NS-13, *MZ*). (c) Tiny titanite grains coexisting with titano-magnetite and ilmenite lamellae (Sample NS-36, *LZa*). (d) Partial enlarged drawing in (c). The white local area is magnetite and the grey spot is titanite (Sample NS-36, *LZa*). (e) and (f) Some of the titano-magnetite was totally replaced by titanite (Sample NS-39, *LZa*). The BSE of ilmenite occur as: (g) Euhedral granular ilmenite (Sample NS-20, *MZ*); (h) Ilmenite edge aound titanite (Sample NS-08, *UZ*); (i) Comb-like ilmenite, the interconnected voids filled with chlorites, albite, quartz and a bit of zircon (Sample NS-22, *MZ*); (j) Acicular ilmenite (Sample NS-30, *MZ*); (k) Ilmenite exsolution lamellae within titano-magnetite (Sample NS-33, *LZb*). (l) The interstitial calcite should be noted (Sample NS-18, MZ).Pl, plagioclase; Cpx, clinopyroxene; Tit-mag, titano-magnetite; Ilm, ilmenite Ttn, titanite; Chl, chlorite; Ap, apatite; Zr, zircon.

an increase in FeO_t and TiO_2, and the diminishing plagioclase reflects the decreasing Al_2O_3. Positive correlations existing between MgO and CaO in *LZa* and the *UZ* closely correspond to clinopyroxene. The increase in silicic mesostasis of quartz and alkali feldspar + quartz assemblages in the *MZ* reflects the increasing SiO_2 and K_2O.

4.2.2. Trace elements

The concentrations of V, Cr, Ni, and Co vary widely, ranging from 30 to 1230 ppm, 26 to 135 ppm, 0.2 to 77 ppm, and 20 to 96 ppm, respectively. The Cr concertations of 105–135 ppm in *LZa* are obviously higher than those (26.3–74.1 ppm) in other layers, whereas elements such as V, Co, and Ni show consistent concave-type variation curves with a spike in *LZb*. The decrease in these elements upward to the *MZ* is related to the low proportion of Fe-Ti oxides and clinopyroxene. *LZb* has a positive Ti anomaly while quartz-bearing gabbro (in *MZ*) has a strong negative Ti anomaly, but such anomalies are inconspicuous in the *UZ* and *LZa*. The whole-rock Sr concentrations, mostly between 100 and 250 ppm, are lower in the *MZ* than those in the other zones. Strong negative Sr and Ti anomalies in the *MZ* indicate that the rocks experienced significant removal of Ca-rich plagioclase and Fe-Ti oxides. The complementary Ti anomalies in the *MZ* and *LZb* indicate that Fe-Ti oxides did not reach saturation in the initial melts, while the irretrievable negative Sr anomaly in the primitive mantle-normalized spidergram (Fig. 6a) may be attributed to the large-scale crystallisation of plagioclase in the

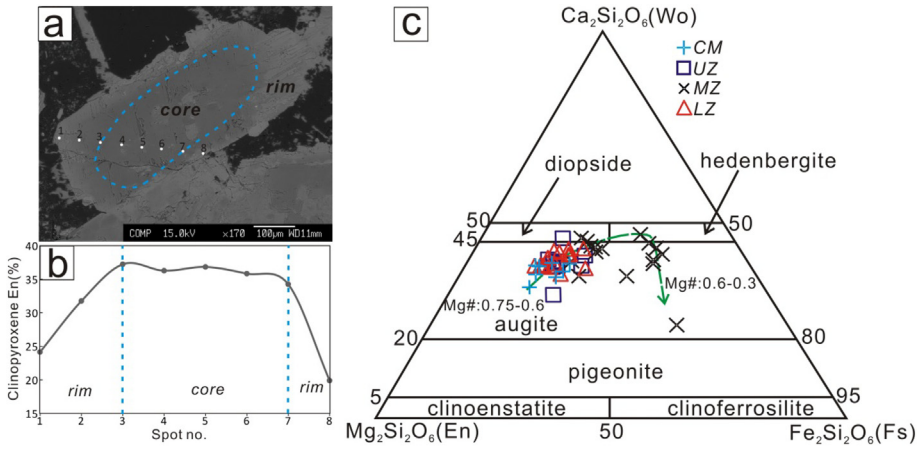

Fig. 5. (a) The normal zoning of clinopyroxene in *LZb* (Sample NT-32, *LZb*). (b) The compositional section in (a). The distance between two spots is 50 μm. (c) The compositional variation of clinopyroxene in units.

earliest magmatic system. The contents of large ion lithophile elements (LILE) (e.g., Rb and Ba) and high field-strength elements (HFSE) (e.g., Th, U, Zr, and Hf) are higher in the *MZ* than those in the overlying *UZ* and underlying *LZ* in the primitive mantle-normalized spidergram (Fig. 6a). The total rare earth elements contents (ΣREE) in the *MZ* (202–305 ppm) are higher than those in the *UZ* (128–152 ppm) and *LZ* (106–120 ppm). The normalized REE curves are almost parallel, and the fractionation between LREE and HREE is weak ($(La/Yb)_N$ = 3.6–4.3) (Fig. 6b). A weak negative Eu anomaly shows in the *MZ* but not in the *UZ* and *LZ* (Fig. 6b). The consistency of trends for so many elements suggests that the sill evolved from a magma or magmas that were very closely related geochemically.

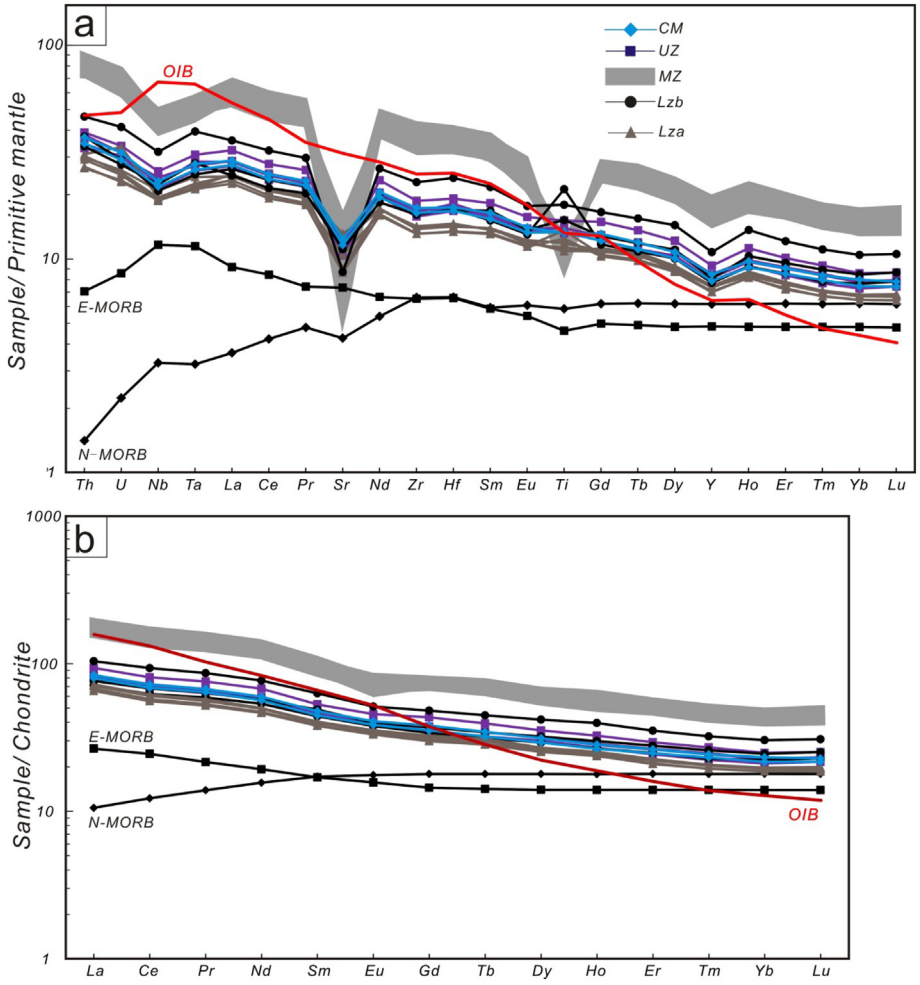

Fig. 6. The compositional variation of trace elements. (a) Primitive mantle-normalized trace element spidergram. (b) Chonride –normalized REE patterns. Primitive mantle and Chonride-normalized values are from Sun and McDonough (1989).

Fig. 3b shows that the highest values for MgO, Cr and the most primitive plagioclase composition occur in *LZa* (−19.4 to −21.8 m), the highest values for FeO_t and TiO_2 occur in *LZb* (−17.7 to −18.7 m), the highest value for P_2O_5 occurs in *LZc* (−16.7 to −17.7 m), and the most enriched incompatible elements occur in the *MZ* (−3.6 to −16.7) (Fig. 6). The uppermost rocks show the near mirror image of the lower section. Thus, the variation for each parameter is different, which indicates control by different processes.

4.3. Thin-section-scale titanite major (EPMA) and trace element chemistry (LA-ICP-MS)

As shown above, titanite can be recognized in three forms: Type 1, subhedral titanite in rocks at the base of the *UZ* (Fig. 4a); Type 2, thin titanite rims on ilmenite, mostly in the *MZ* (Fig. 4b); and Type 3, tiny titanite grains within remanent titano-magnetite in *LZb* (Fig. 4c, d). Titanite EPMA data for two samples are summarized in Supplementary Table 7. The analysed suite includes one sample with subhedral titanite and one tiny titanite with titano-magnetite. Type 1 (Fig. 4a) and Type 3 titanite have similarities in major elements, and both types have high contents of FeO_t (1.5–4 wt%) and Al_2O_3 (1.7–2.6 wt%). This feature occurs because titanite is dominated by the end-member Ca[*TiO*]SiO_4 with combined Fe and Al substitution on the Ti site. Type 1 titanite grains are depleted in rare earth elements and Zr (Fig. 7a); the Zr abundance yields element Zr-in-titanite temperatures ≤618 °C (Supplementary Table 8). Type 1 titanite also has low contents of Sr (18.3–25.9 ppm), Th (0.4–0.9 ppm), and U (0.5–1.5 ppm) with an uncommonly positive Eu anomaly (Fig. 7b).

5. Genesis of the Ti-rich minerals

5.1. Titanite

Titanite is one of the most common titanium minerals in the lithosphere. Generally, titanite grows during late magmatic evolution and under relatively oxidized conditions (Wones, 1989; Xirouchakis and Lindsley, 1998); thus, it has high partition coefficients for Zr, Y, Hf, and REE. Titanite is a common accessory mineral in dolerite/gabbro from the Niutishan mafic sill. In addition to large crystals, this rock contains microscopic crystals of titanite intimately associated with Ti minerals (ilmenite and titano-magnetite). The crystals do not exhibit complex zoning patterns that represent a combination of oscillatory, core-rim, and/or sectorial zoning. The most common variety comprises reaction mantles on ilmenite (Fig. 4b), pseudomorphs after titano-magnetite (Fig. 4e, f) and fracture fillings in ilmenite (Fig. 4a) and titano-magnetite (Fig. 4c). Fracture fillings in titano-magnetite and pseudomorphs after

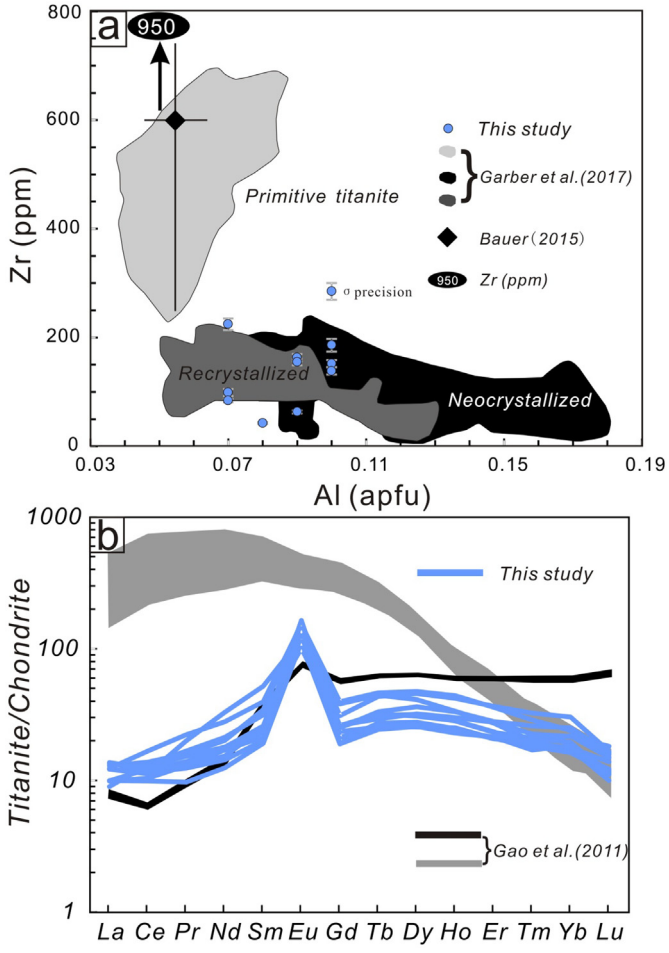

Fig. 7. (a) LA-ICP-MS Zr vs EPMA Al correlations. The prmitive tianite data from Baure (2015) (2SD, $n = 50$) and Gaber et al. (2017). The recrystllized and neocrystallised titanite from Gaber et al. (2017). The blue cycle showing this study (sample NS-08); representative 1σ precision are indicated. (b) Chondrite-normalized REE patterns. The blue lines showing this study. The grey and balck lines in respect showing neocrystallised and retrograde phases were associated with two episodes of fluid activity from Dabie Orogeny (Gao et al.,2011). Chonride-normalized values are from Sun and McDonough (1989).

exsolution lamellae of ilmenite are invariably enriched in Fe (not show). Hence, we speculate that all titanite grains in the sill are not crystallised from the gabbroic melt. Type 1 titanite has much more Al and Fe and less Zr, particularly in REE. The REE normalized patterns exhibit depleted LREE and HREE but relatively higher MREE with positive Eu anomalies (Fig. 7b), which is significantly distinct from those of primitive igneous titanite (Bauer, 2015; Garber et al., 2017) (Fig. 7a). The characteristics also differ from those of fluid-induced metamorphic titanite (e.g., Gao et al., 2011) (Fig. 7b). The positive Eu anomalies and extremely low REE abundances suggest that Type 1 titanite did not crystallise from high-temperature gabbroic melt (as illustrated by the low Zr-in-titanite temperatures) and was not affected by plagioclase fractionation. In most titanite crystals, the important substitutions include Sr, REE, Pb, and U for Ca and Al, Fe^{2+}, Fe^{3+}, Zr, Nb and Ta for Ti (Kohn, 2017), for example:

$$REE^{3+} + (Al, Fe)^{3+} = Ca^{2+} + Ti^{4+}$$
$$Nb^{5+} + (Al, Fe)^{3+} = 2Ti^{4+}$$

The Zr-in-titanite temperature (584 °C),the positive Eu^{3+} anomaly and the irregular boundary of Type 1 titanite, suggest that its crystallisation was restricted to small volumes of rock affected by fluid/melt-induced metasomatism, and might have been controlled by the local major- and trace-element budget. During the late igneous fluid/melt, the Eu^{2+} transformed to Eu^{3+} under oxidizing conditions, and the Eu^{3+} diffused into the fluid/melt.

Type 3 tiny titanite grains within remnant titano-magnetite (Fig. 4c, d) might also be a secondary phase induced by a calcareous fluid/melt. The ilmenite lamellae in titano-magnetite might have provided good channels to allow fluid/melt passage and mass transfer. This interpretation seems to accord with previous studies; for example, titano-magnetite and ilmenite lamellae completely have transformed to titanite in dolerite at Olympic Dam in South Australia (Apukhtina et al., 2015).

Type 2 titanite mostly appears in hydration reactions (e.g., clinopyroxene + ilmenite + quartz + H_2O = amphibole + titanite) and oxidation reactions (e.g., amphibole + ilmenite + O_2 = titanite + magnetite + quartz + H_2O) during amphibolite-facies metamorphism or subsequent greenschist-facies overprinting (Harlov et al., 2006). In most mafic rocks, reactions controlling titanite involve fayalite, ferro-actinolite, hedenbergite and annite in the range of 600–1100 °C (Xirouchakis and Lindsley, 1998; Frost, 2000). However, there is no corresponding reaction formation involving hydrous minerals such as amphibole and biotite. We found some interstitial carbonate (~80 μm) in thin section (Fig. 4l), which could be (1) the most advanced interstitial phase by differentiation (e.g., Bailey, 1993); (2) derived from a carbonated silicate magma by liquid immiscibility (e.g., Le Bas, 1981; Solovova et al., 2005); or (3) captured from the host carbonate rocks during magma emplacement (e.g., Barnes et al., 2005). The most typical petrographic milieu of igneous carbonatites in either intra- or circumcratonic settings includes a broad spectrum of silica-undersaturated mildly to strongly peralkaline rocks, including melilitolites, foidolites and foid syenites (e.g., Chakhmouradian et al., 2008; Gwalani et al., 1993). Foid-bearing and melilitic rocks have not been documented either at Niutishan village or anywhere in its vicinity, but itself, is not sufficient to assert the assimilative nature of the interstitial calcite in question (see in Chakhmouradian et al. (2008)). Recent studies reported that primary diamond (I b-Type) occurred in the 912–914 Ma (SIMS Pb-Pb baddeleyite age) dolerite sills around the Lan'gan area, thus, the primary magma was likely derived from the lithosphere-asthenosphere boundary over a range of intermediate fO_2 values to support the growth of diamond. Therefore, we further proposed that the interstitial calcite is an ultimate product of the igneous evolution in the sill, responsible for the formation of titanite. But we still cannot rule out that the interstitial calcite was assimilated from host carbonate by mafic magma at high temperature. In any case, carbonate assimilation was possible because CO_2 escaped from the system (Barnes et al., 2005). In mafic rocks, titanite stability is controlled more by the conditions of crystallisation than by bulk compositions (Frost, 2000). Titanite can participate in mineral-mineral, mineral-melt, and mineral-fluid equilibria that can be extremely sensitive to changes in intensive parameters such as temperature, oxygen fugacity, and fluid composition (e.g., Hunt and Kerrick, 1977; Xirouchakis and Lindsley, 1998). We conclude that the titanite in the sill formed during the late evolutionary stages as products of reaction between the primary Ti minerals and a late igneous fluid/melt at temperatures near 584 °C:

$2FeTiO_3 + 1/2O_2 + 2CaCO_3$ (in residual fluid/melt) + $2SiO_2$ = $2CaTi[SiO_4]O$ (Type 2 titanite) + Fe_2O_3 + $2CO_2$ (Cassidy and Grove, 1988).

CO_2-rich fluid/melt + CaO + SiO_2 + Fe-Ti oxides→Titanite (Type 1 and Type 3).

The formation of titanite is expected. Excess SiO_2 is also present in quartz-bearing gabbro. This process also affected the rock-forming mafic silicates (particularly chlorite), leading to release of a substantial amount of Ca, Mg, Fe, Ti, and Al into the fluid.

5.2. Ilmenite

Various ilmenite grains occur as (1) euhedral-tabular (Fig. 4g) forms; (2) ilmenite edges on titanite (Fig. 4h); (3) honeycomb (Fig. 4i); (4) acicular ilmenite (Fig. 4j); (5) ilmenite lamellae within titano-magnetite (Fig. 4k); and (6) ilmenite edges around titano-magnetite (Fig.4c). For all such diversity, the ilmenite grains share similar compositions, with MnO and MgO contents of 1.6–2.3 wt% and 0–0.26 wt%, respectively (Supplementary Table 6). Tabular euhedral ilmenite might crystallise from magma or intercumulus phases. Two types of ilmenite lamellae seem to occur in two generation; i.e., the first larger sandwich-type lamellae and the second finer-grained, trellis-type lamellae. The former type may be primary and originate at same time as the host titano-magnetite whereas the latter type likely formed under lower temperature and thus, lower diffusion conditions (Mucke, 2003). The comb-like ilmenite reflects its late crystallisation or intercumulus phase affinity, while some comb-like ilmenite coexisting with zircon (Fig. 4i) may signify that its formation temperature was close to the Zr-saturation temperature. The ilmenite rims on titanite (Fig. 4h) in the *UZ* seem to record (1) decreasing fO_2 (Buddington and Lindsley, 1964) or (2) increasing temperature (Colombini et al., 2011) conditions in the magma system.

Ilmenite is a common accessory mineral in mafic and ultramafic rocks of both komatiitic and tholeiitic affinities from low- to high-grade metamorphic domains. Metamorphic ilmenite is distinct from igneous ilmenite especially in MgO and MnO. In general, the content of MnO is <1 wt%, and MgO is <3 wt% in igneous ilmenite from basic rocks (e.g., Haggerty, 1976; Mucke, 2003), while ilmenite in high-Mg basaltic magmas exhibits MgO contents between 4.0 and 10 wt% (Cawthorn et al., 1985). By contrast, metamorphic ilmenite tends to show MnO content of 1.1 to 11.1 wt% and MgO of <0.1 wt%, with X_{pyr} between 2.5 and 10% (Cassidy and Grove, 1988). Ilmenite in this sill has a high content of MnO but very low MgO, indicating that the primary igneous ilmenite might have been modified by post-magmatic diffusion processes because Mn is more likely to diffuse into ilmenite than into silicate minerals under reducing conditions (Andersen and Lindsley, 1979).

5.3. Titano-magnetite

Both magmatic and hydrothermal processes can yield titano-magnetite with distinct paragenetic mineral assemblages and geochemical features. The titano-magnetite from magmatic processes is characterized by: (1) internal ilmenite lamellae (Mucke, 2003); (2) depletion in elements that are highly compatible with hydrothermal fluids (e.g., REE, Si, Ca, Na and P); (3) enrichment in elements considered relatively immobile in hydrothermal fluids (e.g., Ti, Al, Cr, Zr, Hf and Sc); (4) low

Ni/Cr ratios (≤1) and (5) the absence of oscillatory zoning in Si, Ca, Mg, REE and most high field strength elements (Dare et al., 2014, 2015).

The titano-magnetite shows limited ranges of SiO_2 (0.06–0.1 wt%) and CaO (0.07–0.23 wt%). However, most of the primary titano-magnetite has been replaced by titanite (Fig. 4e, f). One possibility might be that Ca and Si were absorbed into primary igneous titano-magnetite and then altered to titanite (Fig. 4c, d). High Ti (7.2–9.7 wt%) and Al (2300–9300 ppm) in titano-magnetite from *LZb* is consistent with magmatic minerals but contrasts with those formed from high-temperature fluids. Crystallisation experiments on basaltic andesite end-member from the 24 ka Lower Pollara eruption (Salina, Aeolian Islands, Italy) demonstrate that the iron-oxides are generally more Ti-rich under reducing conditions (ΔFMQ + 0.1 to ΔFMQ + 1, where FMQ is the fayalite-magnetite-quartz buffer) than under oxidizing conditions (ΔFMQ + 2.2 to ΔFMQ + 3.3) with similar water concentrations (Beermann et al., 2017). This observation is also true of the magnetite in the Niutishan sill, where the fO_2 in the earlier magma system was relatively low (below ΔFMQ-1.7~ − 2.0). The ilmenite lamellae within titano-magnetite (Fig. 2g) imply that the primary Fe-Ti oxides are Ti-rich magnetite because Ti is considered relatively immobile in hydrothermal fluids. The calculated Fe-Ti exchange temperature from the revised Fe-Ti two-oxide geothermometer of titano-magnetite and coexisting thick ilmenite lamellae ranges from 569 to 652 °C. This result may suggest that the primary titano-magnetite was influenced by late igneous fluid/melt. The fO_2 became nearly stable accompanying the temperature decrease from 650 to 570 °C (Fig. 8j). With the progressive evolution of the magma, ilmenite lamellae form from titano-magnetite under relatively slightly higher fO_2 conditions (Fig. 8, Stage 1). Ilmenite lamellae within titano-magnetite might provide good channels to allow fluid/melt passage and mass transfer to form titanite. Titanite might be related to the late igneous fluid/melt induced oxidation events (>ΔFMQ-1.7) under low temperature, which was characterized by the formation of symplectic intergrowths with Fe-Ti oxides as the magma cooled to ~584 °C (Fig. 8, Stage 2). Further, the ilmenite rims around titano-magnetite might be induced by post-igneous reduced fluids. Meanwhile, the reduced fluids have modified the previous ilmenite lamellae (Fig.8, Stage 3) and other types of ilmenite and enriched them in MnO and reduced MgO.

In summary, the mineral assemblage and chemical fingerprint of titano-magnetite and ilmenite suggest a magmatic origin from Fe-Ti-rich melts rather than a hydrothermal model. The Ti-rich magnetite may be an indicator that titano-magnetite is an earlier phase than ilmenite, which affects magnetite composition. For example, in some anorthosite-hosted Fe-oxide deposits, the crystallisation of magnetite after ilmenite would cause relative depletion in elements that preferentially partition into early-forming ilmenite, i.e., Ti (2–6 wt%), Hf, Mg, Mn, Nb, Sc, W, and Zr (Néron, 2012).

6. Petrogenesis of the sill

6.1. The parental magma and the properties of the mantle source

Magmas can be placed into two convenient categories: those that carry phenocrysts upon emplacement and those that do not (e.g., Marsh, 1989). Obviously, the significant internally differentiated layers within the Niutishan sill were formed by a phenocryst-bearing magma because phenocryst-free bodies, especially sheet-like intrusions, are frequently uniform in composition from top to bottom (Namur et al., 2015). Fe- and Ti-rich features show in the chilled margin (Fig. 9). Their whole-rock Mg# of 38–39 is greater than those of other samples except for samples from *LZa*. Considering the similarity of An in plagioclase and Mg# (En) in clinopyroxene between the phenocrysts in the *CM* and crystal grains in *LZa* (Fig. 3b), we suggest that such an affinity indicates that they are derived from the same magma. *LZa* may represent a clinopyroxene-dominant accumulation, as illustrated by its highest value for Cr. Moreover, the normal En and Mg# zoning of Cpx in *LZb* (Fig. 5) shows evidence of the mechanical settling process for the crystals. Thus, *LZa* is not a true measure of the original magma. We suggest that the *CM* can nearly represent its parental magma because the margin of the sill records only limited crystallisation during flow compared to the other more evolved components. Given the Mg# of <45 and extremely low Cr-Ni contents compared to primitive mantle-derived magmas, the parental magma is far from a typical primary magma but indicates an evolved one. Generally, primary Fe-Ti-rich basalts are scarce on the crustal surface because they are too dense to transport over long distance from mantle depths to the surface, and sometimes Fe-Ti-rich liquids mix with replenished magmas that dilute the concentrations of Fe and Ti (Brooks et al., 1991). However, some picrites and ferro-picrites in large igneous provinces (e.g., Pechenga and Deccan) are regarded as having the characteristics of mantle-derived primary magmas and of a petrogenetic relation with mantle plume head melting (Gibson et al., 2000; Hanski and Smolkin, 1995). We suggest that the tholeiitic parental magma of the sill, similar to the parental magmas of the Skaergaard and Sept Iles layered intrusions, contained less FeO_t from the start and did follow the trend of Fe enrichment.

There are widespread ~900 Ma mafic dykes and sills across the craton (Peng et al., 2011a, 2011b; Wang et al., 2012; Zhang et al., 2016), and some of them contain a high-Fe-Ti component that is similar to the Niutishan sill (Table 1). The Dalian and Sariwon sills are two coeval complexes that have ages close to that of the Chulan sill complex along the south-eastern NCC (Fig. 1). These sills have similar mineral assemblages (Table 1) and chemical composition, e.g., major and trace element concentrations, trace element patterns and Sr-Nd isotopes (Peng et al., 2011b). Thus, the three swarms might be part of a coeval large sill swarm. The primitive mantle-normalized and chondrite-normalized REE patterns indicate that the magmas had primary melt compositions similar to those of *E*-MORB to oceanic island basalts (OIB) (Fig. 6) but less prominent low LILE/LREE ratios. These rocks exhibit high initial $^{87}Sr/^{86}Sr_{(t=900\ Ma)}$ values varying from 0.706 to 0.709 and low $\varepsilon Nd_{(t=900\ Ma)}$ values ranging from −1 to −6 (Peng et al., 2011b) and define a trend that lies between EM I (enriched mantle I) and EM II (enriched mantle II) (see Peng et al., 2011b, Fig.6), which implies an ancient continental lithospheric mantle source or slightly enriched mantle source. The ferro-basaltic parental magma properties and tholeiitic rocks from the Niutishan sill are unlike of those from an arc system, which produces hydrous magmas (2–6 wt% H_2O, see in Plank et al. (2013)) and is responsible for the entire range of crystallisation trends from tholeiitic to calc-alkaline (Zimmer et al., 2010), because magmatic H_2O-saturated conditions trigger the early crystallisation of Fe oxides and suppress plagioclase on the liquid line of descent (Sisson and Grove, 1993; Zimmer et al., 2010).

6.2. Differentiation controlled by magma immiscibility?

Silicate liquid immiscibility is very common in most tholeiitic layered intrusions (e.g., Panzhihua, Sept Iles, Skaergaard, Bushveld, Duluth, Bjerkreim-Sokndal, Sudbury, Stillwater) or volcanics (Jakobsen et al., 2005; Namur et al., 2012; Philpotts, 1982) and can therefore be considered an important process of magma differentiation and has been proposed as explaining the absence of intermediate compositions in volcanic tholeiitic provinces (Charlier et al., 2013). Contrasting melt inclusions trapped in cumulus phases provide the most obvious record for the coexistence of equilibrium paired melts, as described in the Skaergaard intrusions (Jakobsen et al., 2005). When a liquid line of descent of homogeneous melts reaches a binodal surface, two contrasting liquids are produced. Iron-rich magma could fall while silica-rich magmas rise depending on the density contrast (Hunter and Sparks, 1987; Veksler et al., 2006, 2007). This process may lead to the complete dissolution of some cumulus minerals and the formation of the monomineralic layers (Veksler and Charlier, 2015). The resultant FeO_t and TiO_2 in Fe-rich magma can be as high as 30 wt% and >2 wt%,

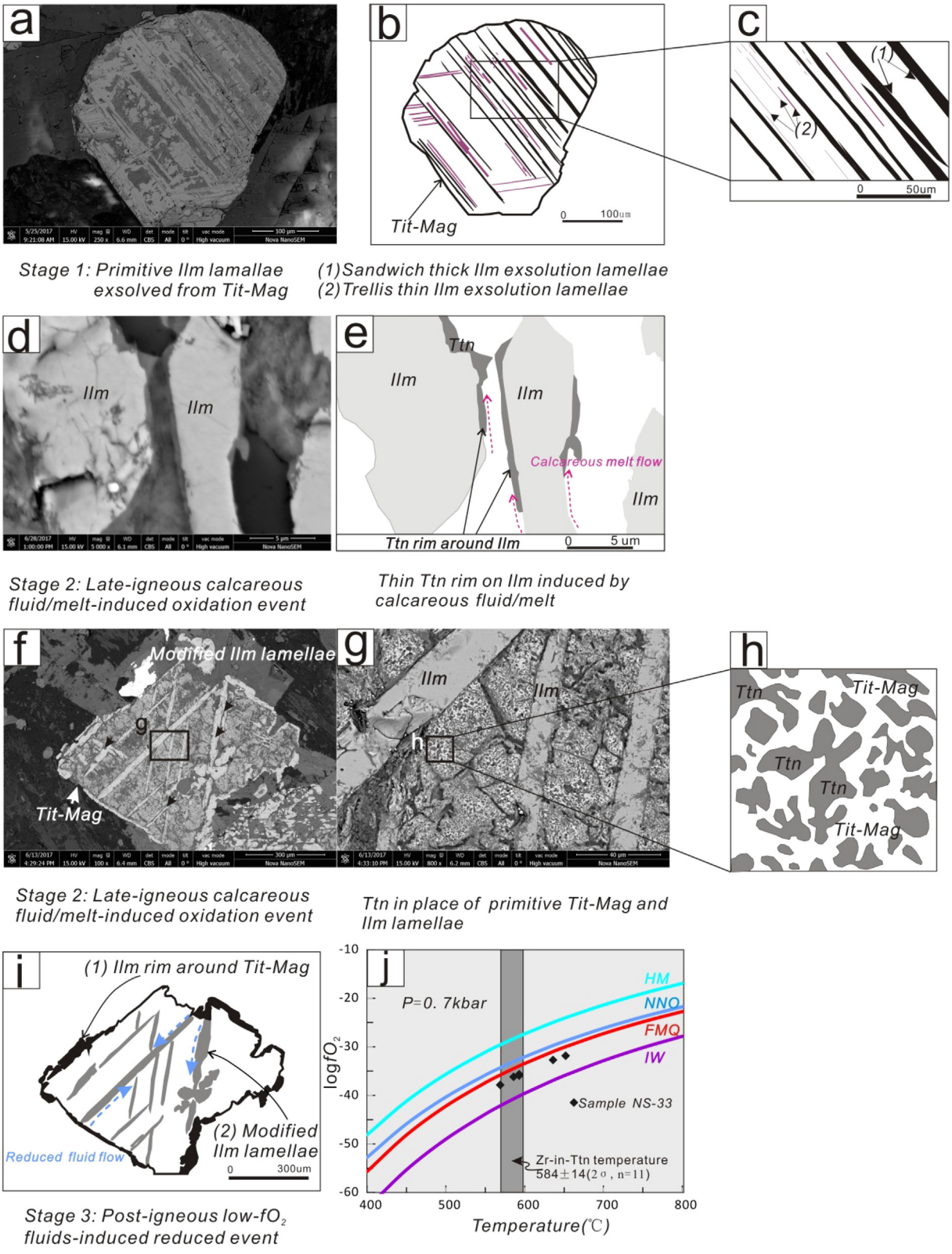

Fig. 8. The plot of Fe-Ti oxides texture modified by two period fluids. (a) Ilmenite exsolution lamellae within titano-magnetite (Sample NS-33, *LZb*). (b) The cartoon of two period of ilmenite lamellae in (a). (c) Partial enlarged drawing in (b). A cartoon showing two kind of ilmenite exsolution lamellae. The red lines represent trellis intergrowths thin lamellae (≤1 μm) and the black lines represent sandwich intergrowth thick ilmenite lamellae (3–7 μm). (d) The photomicrograph showing secondary tiny titanite rim (≤1 μm) around ilmenite induced by high-fO_2 fluid in the terminal period of magma evolution (Sample NS-13, *MZ*). (e) The cartoon of titanite thin edge on ilmenite. (f) Previous titano-magnetite altered to titanite (Sample NS-36, *LZa*). (g) Partial enlarged drawing in (f). (h) The cartoon of partial enlarged drawing in (g). The tiny titanite should be noted. The white local area is titano-magnetite and the grey spots are titanite (Sample NS-36, *LZa*). (i) The ilmenite rim around titano-magnetite induced by reduced post-magmatic fluid (Sample NS-36, *LZa*). (j) Log fO_2-T diagram caculated by the Fe-Ti oxide geothermobarometer. The seleceted Fe-Ti oxides pair is the titano-magnetite and coexting ilmentite thick lamellae in sample NS-33. Four oxygen reference buffers-FMQ (fayalite-magnetite-quartz), NNO (Ni-NiO), IW (iron-wustite) and HM (magnetite-hematite) - are plotted for comparison.

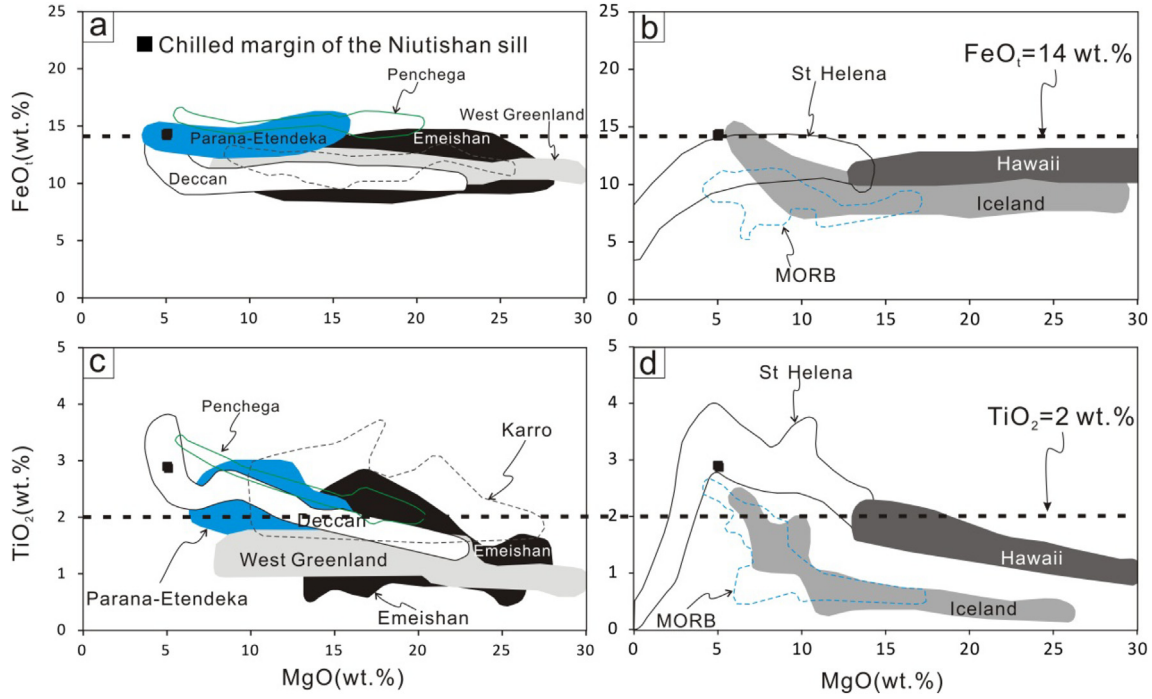

Fig. 9. Comparison of MgO vs. FeO_t and MgO vs. Ti_2O contents in ferro-basalts from the Niutishan sill chilled margin (Table 2) with: (a) and (c) Selected continental flood ferro-picrites and high-iron basalts from Deccan, Emeishan (Data from GEOROC), Parana-Etendeka (Gibson et al., 2000), Pechenga (Hanski and Smolkin, 1995), Karro (Cox and Jamieson, 1974) and West Greenland (Holm et al., 1993). (b) and (d) Selected ocean island ferro-picrites from Hawaii, Iceland, St Helena and mid-ocean ridge basalts (Data from GEOROC).

respectively. Phosphorus is more compatible in a Fe-rich liquid relative to its conjugate silicic fraction ($Kd_P^{\text{Fe-rich melt/silicic melt}} \approx 8–9$). REEs show a greater affinity for Fe-rich liquid ($Kd_{REEs}^{\text{Fe-rich melt/silicic melt}} \approx 10$) than P (Schmidt et al., 2006). From Figs. 3b and 6b, it is obvious that the rocks show quite the opposite character: the quartz-bearing gabbro has higher contents of P_2O_5 and total REE than the underlying Fe-Ti oxide-rich rocks. Moreover, the reactive microstructures between immiscible Fe rich melts and cumulus primocrysts such as those described in the Skaergaard intrusion (Holness et al., 2011) are not observed in *LZa*. Thus, the pronounced internal differentiation cannot be produced by magma immiscibility. The F-rich and Cl-poor apatite ($X_F > 0.95$) and Ti-rich magnetite (7.2–9.7 wt% Ti) from Fe-Ti (P)-rich layers indicate a magmatic origin from the high-temperature Fe-Ti-rich melts rather than a hydrothermal model (Dare et al., 2014; Dymek and Owens, 2001). Thus, the high-Fe-Ti (P) layers may be attributed to the gravitational sinking of Fe-Ti oxides in liquids. Chromium is more compatible in magnetite than in clinopyroxene in mafic melts [$Kd_{Cr}^{Mt/melt} = 153$; $Kd_{Cr}^{Cpx/melt} = 34$, (Rollinson, 1993)]. The higher Cr content in *LZa* than in the overlying *LZb* thus indicates that clinopyroxene crystallised earlier than titano-magnetite in the high-Fe/Ti parental magma. The relative crystallisation sequence among these phases may suggest that the early magma differentiation has been occurred under low fO_2 and water-unsaturated conditions (see discussion below). Conditions such as low water content (Botcharnikov et al., 2008; Charlier and Grove, 2012), lower pressure (Villiger et al., 2006), low oxygen fugacity (Brooks et al., 1991; Philpotts, 1982) and lower cooling rate (Jakobsen et al., 2005; Namur et al., 2012) are conducive to triggering magma immiscibility. The lack of magma immiscibility here may be due to the rapid cooling rate for its thin width (~30 m) and shallow depth (2 km).

6.3. Formation of the Fe-Ti oxide-rich and P-rich layer

Significantly negative Sr anomalies are pervasive in all the samples, particularly so in the *MZ* (Fig. 6a), indicating that plagioclase is an earlier liquidus phase in this shallow sheet-like magma chamber. The highest values for Cr and CaO in *LZa (massive gabbro)* suggest that the crystallisation of Fe-Ti oxides is delayed to lower temperature and that these oxides become liquidus phases after clinopyroxene does. We therefore propose that Fe-Ti oxides were not saturated in the initial magma. Whole-rock and mineral compositions demonstrate that plagioclase and clinopyroxene controlled the liquid line of descent in the early stage (Fig. 10a, b). The low-MgO and evolved high-Fe/Ti parental magmas imply that their compositions evolved along chemical trends driven by higher temperature, olivine-dominant crystal fractionation in a deep-seated magma chamber (Fig. 10). After this stage, the magma ascended, was emplaced in the shallow crust and evolved under lower temperature conditions, with increased proportions of plagioclase and clinopyroxene in the crystallising assemblage (Fig. 11). Significantly, the saturation of Fe-Ti oxides after clinopyroxene and plagioclase in the liquids is distinct from the typical mineral crystallisation sequence (Charlier et al., 2008; Namur et al., 2010) in most high-Fe/Ti tholeiitic magma chambers (Table 3).

The crystallisation order of titano-magnetite in mafic magmas is mainly controlled by the composition of the parental magma, the oxygen fugacity and the volatile content. Toplis and Carroll (1995) conducted 1 atm dry experiments on a Skaergaard-like composition (SC1), and Snyder et al. (1993) performed 1 atm dry experiments on an evolved ferro-basalt related to the Newark Island intrusion (4-83C). The former showed that magnetite crystallises later, probably after clinopyroxene under oxidized conditions below $\triangle FMQ + 1.5$, while the latter showed that the Fe-Ti oxides crystallise earlier than clinopyroxene under similar conditions of pressure and fO_2. Namur et al. (2010) proposed that low CaO/FeO_t and CaO/TiO_2 ratio values in the composition of the primary magmas could be the key parameter controlling the relative order of crystallisation between Fe-Ti oxides and clinopyroxene. When CaO content is relatively low and FeO_t and TiO_2 contents are higher, Fe-Ti oxides could be saturated earlier than clinopyroxene. The parental magma of the Niutishan sill is intermediate between SC1 and 4-83C in terms of CaO/FeO_t and CaO/TiO_2 ratios and the TiO_2/CaO and FeO_t/CaO are

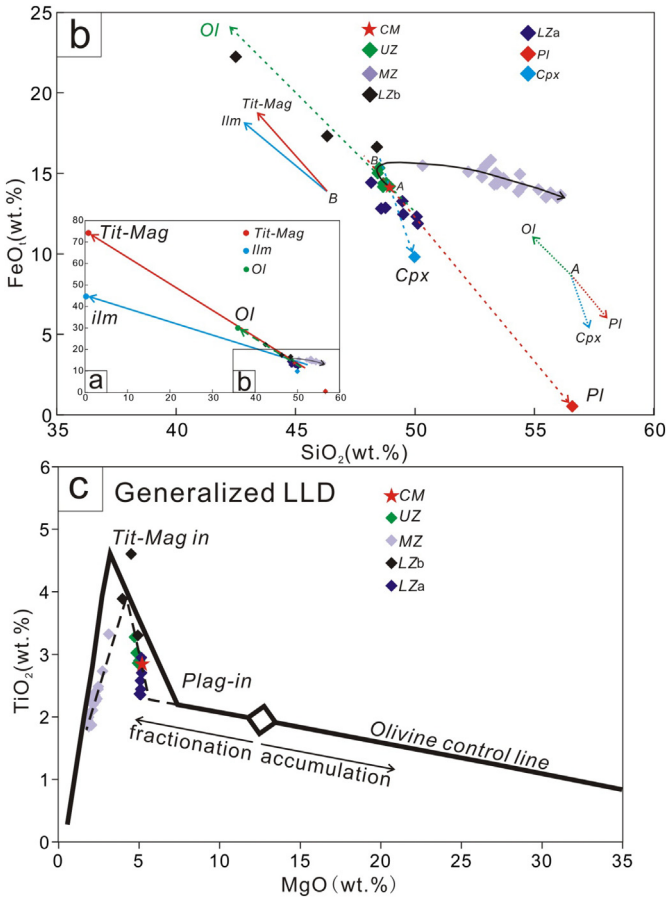

Fig. 10. Plots of (a) SiO_2 vs. FeOt. the Tit-Mag value is the average composition of titano-magnetite in sample NS-33 ($n = 6$, *LZb*); The Ilm value is the average composition of euhedral ilmenite in sample NS-33 ($n = 2$); the Ol value is the averge composition of olivine in MCUI, Sept Iles intrusion ($n = 3$, Namur et al., 2010). (b) Partial enlarged drawing in (a). the Pl value is the average composition of plagioclase in sample NS-32 to 40 ($n = 19$, *LZ*); The point A represent the compsion of chilled margin (parental magma); the point B represent the sample NS-09 in the bottom of the *UZ*. (c) Cartoon of a typical liquid line of descent (LLD) for a primary OIB composition in which plagioclase is cotectic before titano-magnetite saturation (Prytulak and Elliott, 2007). Pl, plagioclase; Cpx, clinopyroxene; Ol, olivine; Tit-Mag, titano-magnetite; Ilm, ilmenite.

higher than those for the Sept Iles intrusion. In theory, a relatively high FeO_t and TiO_2 parental magma such as the Niutishan sill can produce the Sept Iles sequence of crystallisation, but the Fe-Ti oxides are still the later phases to appear (Table 3). Therefore, the order of crystallisation in the Niutishan sill between clinopyroxene and magnetite was not controlled by CaO/FeO_t and CaO/TiO_2 ratios in the parental magma.

The relative crystallisation sequence among these phases is also dependent on H_2O contents; thus changes in crystallisation assemblages may also in part reflect coupled temperature and H_2O content. Petrologic experiments suggest that high a_{H_2O} results in the crystallisation of Fe-Ti oxides prior to clinopyroxene and leads to rapid decreases in Fe and Ti during magma evolution (Snyder et al., 1993; Botcharnikov et al., 2008; Beermann et al., 2017;). Botcharnikov et al. (2008) showed that magnetite is the first liquidus phase in oxidized conditions above ΔFMQ + 1.5 and the third phase earlier than plagioclase between ΔFMQ + 1.5 and ΔFMQ under water-saturated conditions. Due to the scarcity of hydrous phases such as biotite and Ca-rich amphibole, we suggest that the ferro-basaltic parent magma of the Niutishan sill did not contain considerable water. Mechanical settling of clinopyroxene primocrysts from the initial parental magma formed the more primitive Cpx-rich mush on the floor (*LZa*), as indicated by the highest MgO, Cr and CaO concentrations (Fig. 3). The earlier fractional crystallisation of Pl + Cpx under water-unsaturated conditions made the residual magma rich in Fe and Ti. The downward increase in FeO_t, TiO_2 and Cpx Mg# within the *UZ* may reflect this fractional process. After the saturation and mechanical settling of clinopyroxene primocrysts from the initial parental magma, large amounts of Fe-Ti oxides crystallised from the residual Fe-Ti-rich (as illustrated by highest values for Ni, Co and V) melt. Further crystallisation and solidification of the crystal mush led to the formation of major Fe-Ti oxide-rich layer in the lower zone of the intrusion (Fig. 11b) and expelled interstitial residual melt upward to mix with the more evolved melts, leading to the saturation of apatite. This behaviour is in agreement with the experimental data of Toplis et al. (1994), indicating that the crystallisation of magnetite lowers the solubility of phosphorus in basaltic melts. Thus, the origin of the Fe-Ti oxide-rich layer in the sill is attributed to a vertical crystal mechanical sorting process. This process is mostly efficient in basaltic magma systems, which is due to the low viscosity (close to Newtonian) of the melt and the significant density contrasts between phases and melt (Namur et al., 2015). Thus, that the highest FeO_t and TiO_2 contents occur in *LZb* is interpreted as the result of mechanical accumulation of Fe-Ti oxides.

6.4. Formation of the quartz gabbro (MZ)

We here discuss the processes that may have produced the trends in relative values of incompatible elements such as REEs and Na_2O, considered to be a result of the accumulation of plagioclase, clinopyroxene and Fe-Ti oxides (no olivine). The partitioning of an incompatible element into one of the early phases has very little effect (Cawthorn et al., 2017). As the solidification fronts gradually move inward during

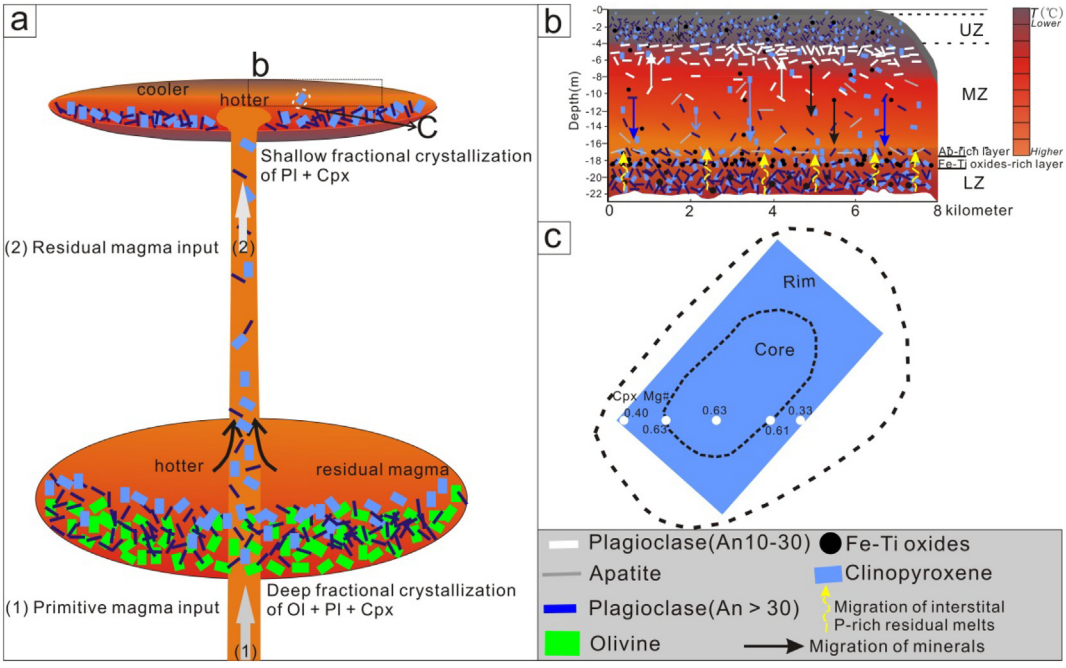

Fig. 11. Schematic illistrations of the Niutishan mamga system. (a) The compositonal evolution of the doleriteic rocks are representd by shallow fractional crystallisation of clinopyroxene + plagiocalse; the parental magma derived from a deep-seated magam chamber, which has experienced earlier-fractionated crystals of primitive olivine, plagiocalse and clinopyroxene. (b) Mechanical settling of clinopyroxene and plagioclase primocrysts from the initial magma followed by large amounts of Fe-Ti oxides. Further crystallisation and solidification of the crystal mush led to the formation of the major Fe-Ti oxide-rich layer in the lower zone of the intrusion and expelled more evolved melt upward, leading to the saturation of apatite. The saturation of apatite and albite-oligoclase produces new liquidus phases in the more evolved residual magma after rapid removal of the Fe-Ti oxides by density contrast. As a result, viscosity would increase, restricting the separation of liquid from early crystals. The essentially changes in the compositions and proportions of trapped liquid controlled the mineral chemistry in the more advanced residual magma mush. It would seem simple to produce compositional diversity by the combined processes of fractionation, accumulation and compaction in this magma system. (c) The normal-zoning of clinopyroxene in *LZ* (Sample NS-32, *LZb*). Dashed lines represent boundaries of zones.

cooling, crystal ensembles are nucleated and continue growing until the solidus isotherm arrives when all melt has been consumed (controlled by the rate of diffusive heat loss through the walls). A series of small decoupled Fe-P signatures within the *UZ* (Fig. 4b) may record the development of solidification fronts with time. The compositions of quartz gabbro in the *MZ* agree well with the clinopyroxene-plagioclase-Fe-Ti oxides fractionation trend (Fig. 10a). A significant decrease in abundances of MgO, CaO, Al_2O_3, FeO_t and TiO_2 on the one hand, and V, Cr, Ni and Co on the other, is consistent with early removal of mafic silicate, plagioclase and Fe-Ti oxides from the parental magma. This conclusion is in accord with the presence of cumulate clinopyroxene-plagioclase (*LZa*) and Fe-Ti oxides (*LZb*) units in the low parts of the sill. The saturation of apatite and albite-oligoclase produces new liquidus phases in the more evolved residual magma after rapid removal of the Fe-Ti oxides by density contrast. A drop in P_2O_5 content, coupled with depletion in CaO toward the high-silica group (Fig. 3b), indicates removal of apatite. As a result, viscosity would increase, restricting the separation of liquid from early crystals and increasing the bulk partition coefficients of incompatible elements. From −4.5 to −16.7 m height, the magma is fractionating, decreasing in MgO, TiO_2 and FeO_t and significantly increasing in SiO_2, Na_2O and REEs. In terms of the fractionation process, the samples at the base of the *MZ* represent the end of crystallisation of the entire 22 m profile. A plgioclase An decrease to 2 at −6 m and ultimately increase to 56 at the top of the *MZ* is envisaged. It is not possible to demonstrate such changes in bulk partition coefficients, but essentially, changes occur in the composition and proportion of trapped liquid. It would seem simple to produce compositional diversity by the combined processes of fractionation, accumulation and compaction. A Basal solidification front growing upward on the floors of magma chambers can become so thick or distended that their weight is enough to squeeze out the interstitial melt (Marsh et al., 2013). Therefore, compaction of unconsolidated basic crystal mushes can drive extraction of more differentiated interstitial silicic melt (Berger et al., 2017). The quartz and alkali feldspar suite (Fig. 2d) in the *MZ* and its interstitial nature suggest that it is an intercumulus phase of high-silica residual magma, which nucleated and grew in abundant pores in the mush. This process is due to the increasing

Table 3
Some compared ferrobasaltic parent magma compositions with this study and the respective mineral crystallisation sequence.

Composition	SiO_2	TiO_2	Al_2O_3	FeO_t	MnO	MgO	CaO	Na_2O	K_2O	P_2O_5	ASI*	TiO_2/ CaO†	FeO_t/ CaO‡	Crystallisation sequence
	wt%										The value of ratio			(If $\Delta\log fO_2 < \Delta FMQ + 1.5$)
This study	48.95	2.90	12.71	14.17	0.24	5.04	8.91	3.40	0.51	0.30	0.57	0.33	1.59	Pl + Fe-poor Cpx – Fe-Ti oxides + Fe-rich Cpx – Ap;
Sept Iles intrusion	48.56	2.85	14.50	14.87	0.24	5.47	9.71	2.78	0.78	0.57	0.63	0.29	1.53	Ol + Pl – Fe-Ti oxides – Ca-rich Cpx – Ap;
SCI (in dry)	48.80	2.90	14.90	14.60		4.80	10.00	2.90	0.48		0.63	0.29	1.46	Ol + Pl – Cpx – Fe-Ti oxides;
4-83C (in dry)	46.20	3.83	13.40	17.33	0.22	4.66	7.58	3.56	1.03	0.35	0.65	0.51	2.29	Ol + Pl – Fe-Ti oxides – Cpx;
SCI (X_{H_2O}=1)	48.34	2.86	14.61	12.91		6.40	10.87	2.60	0.30		0.60	0.26	1.19	Cpx + Ol – Fe-Ti oxides – Pl – Am;

ASI*: (alumina saturation index) molar ratio of $Al_2O_3/(Na_2O + K_2O + CaO)$.
$TiO_2/CaO^†$: molar ratio of TiO_2/CaO; $FeO_t/CaO^‡$: molar ratio of FeO_t/CaO.
Data sources: Sept Iles intrusion (Namur et al., 2010); SCI (in dry) (Toplis and Carroll, 1995); 4-83C (Snyder et al., 1993); SCI (X_{H_2O}=1) (Botcharnikov et al., 2008).
Ol, olivine; Pl, plagioclase; Cpx, clinopyroxene; Ap, apatite; Am, amphibole.

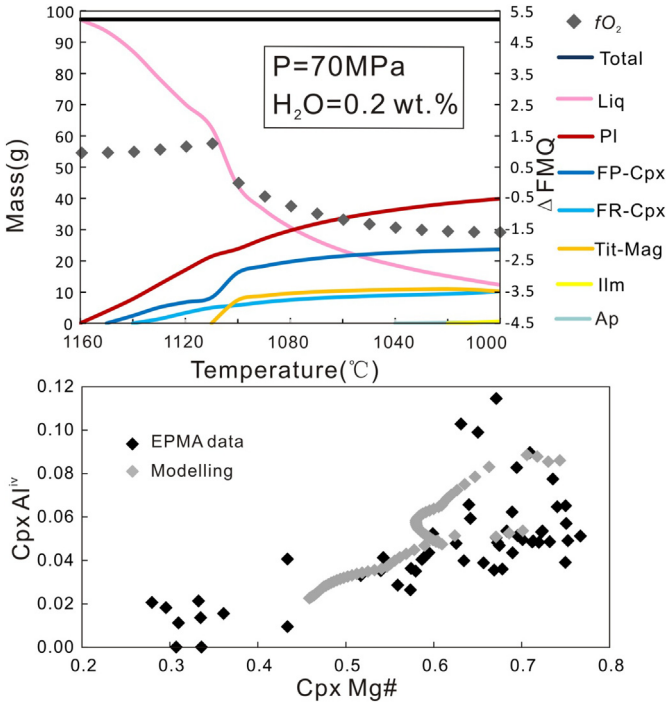

Fig. 12. Graphics displaying the results of an isobaric sequence of calculations. The temperature range from 1200 to 780 °C, in 5 °C steps, at 70 MPa, with fO_2 unconstrained along the FMQ oxygen buffer. (a) Variation in mass as a function of temperature for all phases present, for all solids, and for the whole system (Gualda and Ghiorso, 2015). (b) Plots of Al^{iv} vs. Mg# in clinopyroxene. The black rhombuses represent EPMA values and the values of the grey rhombuses are calculated from MELTS. Liq, liquid; Pl, plagioclase; FP-Cpx, Fe-poor clinopyroxene; FR-Cpx, Fe-rich clinopyroxene; Tit-Mag, titano-magnetite; Ilm, ilmenite; Ap, apatite.

viscosity of the differentiating magma, which traps highly evolved melts and impedes liquid separation.

Large- to moderate-scale magma chambers (e.g., Sept Iles, Skaergaard, and Stillwater) are not formed instantaneously from a single magma pulse of uniform composition but usually include multiple magma additions (Cawthorn, 2015; Kruger et al., 1987; Maier et al., 2012; Namur et al., 2010) in short pulses; thus, lateral magma flow is usually very common during the formation of mafic sills (Magee et al., 2016). However, there is no obvious differentiation along the lateral orientation within outcrop scale in this sill. Given the continuous range of rock types and features in terms of texture, mineral proportions, composition and morphology, the internal differentiated components within the sill were mainly controlled by a vertical mechanical settling process. Lateral magma flows may have played an unimportant role in the formation of the small-scale sheet-like body.

6.5. The crystallisation sequence in the sill and thermodynamic modelling based on MELTS

The parental magma of the Niutishan sill represents an evolved residual magma derived from a deep-seated magma chamber. The crystallisation sequence is plagioclase (An>30) and Fe-poor clinopyroxene followed by Fe-Ti oxides and Fe-rich clinopyroxene, and finally apatite and albite to oligoclase. The initial magma in the sill progressively evolved along an Fe enrichment trend and formed the Fe-Ti oxide-rich layer. However, large amounts of Fe-Ti oxides crystallised from the Fe-rich melt and expelled interstitial P-rich melt upward, leading to the saturation of apatite and more evolved composition. The crystallisation sequence and Fe-Ti-rich features indicate that both the low-fO_2 and water-unsaturated conditions in the earlier magma system are required. Tholeiitic magmas under such conditions were likely not affected by any subduction-related process (Plank et al., 2013; Sisson and Grove, 1993; Zimmer et al., 2010) but formed in an intra-continental environment.

The thermodynamic modelling software MELTS is a powerful tool for investigating crystallisation and melting in natural magmatic systems (Gualda and Ghiorso, 2015). In Fig. 12, we show graphics illustrating the result of a calculation performed for a composition representative of the parental magma in the Niutishan sill (Sample NS-01), with a low H_2O content of ~0.2 wt% to ensure water-unsaturated conditions and fO_2 unconstrained to the FMQ oxygen buffer, in a temperature range from 1200 to 780 °C in 5 °C steps and at a pressure of 70 MPa. In Fig. 12a, plagioclase and Fe-poor clinopyroxene are the first liquidus phases when temperature cools to 1160 °C, and followed by Fe-rich clinopyroxene and titano-magnetite, then apatite and ilmenite and finally oligoclase. The fractional crystallisation with the successive appearance of liquidus phases calculated from MELTS is nearly consistent with what we suggested for the Niutishan sill. The compositional variation in clinopyroxene is also similar to the result of thermodynamic modelling (Fig. 12b). Thus, it is possible to combine a sequence of calculations into an evolutionary path.

7. Conclusions

A being mined stone-pit in the Xuzhou area of North China revealed a ~22-m-thick doleritic intrusion, leaving a section of ~22 m thick is considered to have crystallised as a single entity. This study shows that the conditions of crystallisation in the mafic intrusive rocks influence both the csystallising mineral assemblage and the detailed chemical evolution of phases during differentiation and cooling. The sill crystallised from a ferro-basaltic parent magma under low X_{H_2O} and fO_2 conditions. The highest MgO, Cr and the most primitive plagioclase composition occur in the *LZa*, the highest value for FeO_t and TiO_2 occur in the *LZb* and the highest value for P_2O_5 occurs in *LZc*, revealing a continuous fractional crystallisation of plagioclase and clinopyroxene followed by Fe-Ti oxides, and finally apatite and albite to oligoclase. The crystallisation of plagioclase and clinopyroxene during the early stage induced a Fe-Ti-rich residual magma. Large amounts of Fe-Ti oxides crystallised from the Fe rich melt and accumulated at the lower part of the sill, which

expelled residual melt upward, leading to the saturation of apatite. Further crystallisaion and solidification of the crystal mush led to the formation of the major Fe-Ti oxide-rich layer in the lower zone of the sill. The incompatible elements increased in abundance in the *MZ* are due to the increasing viscosity of the differentiating magma, which traps highly evolved melts and impedes liquid separation. The ~900 Ma significantly differentiated Niutishan sill was produced by fractional crystallisation under closed and anhydrous conditions, reflecting an extensional regime or intracontinental rift.

Acknowledgments

This study was financially supported by the NFSC Project (41772192) and the Advanced Science Key Research Project of CAS (QYZDB-SSW-DQC04281712250). Xiangdong Su thanks Prof. Xiaohui Zhang for the helpful suggestions. We acknowledge the assistance of Di Zhang and Dr. Qian Mao during the microprobe analysis. Wenjun Li and Binyu Gao are thanked for their assistance during ICP-MS analysis. Prof. Yueheng Yang and Rui Li provided help during the LA-ICP-MS analysis. Prof. Shuanhong Zhang and an anonymous reviewer are thanked for their constructive reviews.

Appendix A. Supplementary data

Supplementary data to this article can be found online at https://doi.org/10.1016/j.lithos.2018.08.023.

References

Andersen, D.J., Lindsley, D.H., 1979. The olivine-ilmenite thermometer. Proc. Lunar Planet. Sci. Conf. 10th, pp. 493–507.
Apukhtina, O.B., Kamenetsky, V.S., Ehrig, K., Kamenetsky, M.B., McPhie, J., Maas, R., Meffre, S., Goemann, K., Rodemann, T., Cook, N.J., Ciobanu, C.L., 2015. Postmagmatic magnetite–apatite assemblage in mafic intrusions: a case study of dolerite at Olympic Dam, South Australia. Contrib. Mineral. Petrol. 171, 1–15.
Bailey, D.K., 1993. Carbonate magmas. J. Geol. Soc. 150, 637–651.
Barnes, C.G., Prestvik, T., Sundvoll, B., Surratt, D., 2005. Pervasive assimilation of carbonate and silicate rocks in the Hortavær igneous complex, north-Central Norway. Lithos 80, 179–199.
Bauer, J.E., 2015. Complex Zoning Patterns and Rare Earth Element Variations across Titanite Crystals from the Half Dome Granodiorite, Central Sierra Nevada, California. The University of North Carolina at Chapel Hill, ProQuest Dissertations Publishing M.S. Theses.
Beermann, O., Holtz, F., Duesterhoeft, E., 2017. Magma storage conditions and differentiation of the mafic lower Pollara volcanics, Salina Island, Aeolian Islands, Italy: implications for the formation conditions of shoshonites and potassic rocks. Contrib. Mineral. Petrol. 172.
Berger, J., Lo, K., Diot, H., Triantafyllou, A., Plissart, G., Féménias, O., 2017. Deformation-driven Differentiation during in situ Crystallization of the 2.7Ga Iguilid Mafic Intrusion (West African Craton, Mauritania). J. Petrol. 58, 819–840.
Botcharnikov, R.E., Almeev, R.R., Koepke, J., Holtz, F., 2008. Phase Relations and liquid Lines of Descent in Hydrous Ferrobasalt–Implications for the Skaergaard Intrusion and Columbia River Flood Basalts. J. Petrol. 49, 1687–1727.
Brooks, C.K., Larsen, L.M., Nielsen, T.F.D., 1991. Importance of iron-rich tholeiitic magmas at divergent plate margins: a reappraisal. Geology 19, 269–272.
Buddington, A.F., Lindsley, D.H., 1964. Iron-Titanium Oxide Minerals and Synthetic equivalents. J. Petrol. 5, 310–357.
Cassidy, K.F., Grove, D.I., 1988. Manganoan ilmenite formed during regional metamorphism of Archean mafic and ultramafic rocks from Western Australia. Can. Mineral. 26, 999–1012.
Cawthorn, R.G., 2015. The Bushveld Complex, South Africa. In: Charlier, B., Namur, O., Latypov, R., Tegner, C. (Eds.), Layered Intrusions. Springer Netherlands, Dordrecht, pp. 517–587.
Cawthorn, R.G., Groves, D.I., Marchant, T., 1985. Magnesian ilmenite; clue to high-Mg parental magma of the Insizwa Complex, Transkei. Can. Mineral. 23, 609–618.
Cawthorn, R.G., Chistyakova, S.Y., Latypov, R.M., Kamenetsky, V.S., Danyushevsky, L.V., 2017. A triple S-shaped compositional profile in a Karoo dolerite sill—evidence of concurrent multiple fractionation processes. Geology 45, 603–606.
Chakhmouradian, A.R., Mumin, A.H., Demény, A., Elliott, B., 2008. Postorogenic carbonatites at Eden Lake, Trans-Hudson Orogen (northern Manitoba, Canada): Geological setting, mineralogy and geochemistry. Lithos 103, 503–526.
Charlier, B., Grove, T.L., 2012. Experiments on liquid immiscibility along tholeiitic liquid lines of descent. Contrib. Mineral. Petrol. 164, 27–44.
Charlier, B., Sakoma, E., Sauvé, M., Stanaway, K., Auwera, J.V., Duchesne, J.-C., 2008. The Grader layered intrusion (Havre-Saint-Pierre Anorthosite, Quebec) and genesis of nelsonite and other Fe–Ti–P ores. Lithos 101, 359–378.
Charlier, B., Namur, O., Toplis, M.J., Schiano, P., Cluzel, N., Higgins, M.D., Auwera, J.V., 2011. Large-scale silicate liquid immiscibility during differentiation of tholeiitic basalt to granite and the origin of the Daly gap. Geology 39, 907–910.
Charlier, B., Namur, O., Grove, T.L., 2013. Compositional and kinetic controls on liquid immiscibility in ferrobasalt–rhyolite volcanic and plutonic series. Geochim. Cosmochim. Acta 113, 79–93.
Colombini, L.L., Miller, C.F., Gualda, G.A.R., Wooden, J.L., Miller, J.S., 2011. Sphene and zircon in the Highland Range volcanic sequence (Miocene, southern Nevada, USA): elemental partitioning, phase relations, and influence on evolution of silicic magma. Mineral. Petrol. 102, 29–50.
Cox, K.G., Jamieson, B.G., 1974. The Olivine-rich Lavas of Nuanetsi: a study of Polybaric Magmatic Evolution. J. Petrol. 15, 269–301.
Danyushevsky, L.V., Perfit, M.R., Eggins, S.M., Falloon, T.J., 2003. Crustal origin for coupled 'ultra-depleted' and 'plagioclase' signatures in MORB olivine-hosted melt inclusions: evidence from the Siqueiros Transform Fault, East Pacific Rise. Contrib. Mineral. Petrol. 144, 619–637.
Dare, S.A.S., Barnes, S.-J., Beaudoin, G., Méric, J., Boutroy, E., Potvin-Doucet, C., 2014. Trace elements in magnetite as petrogenetic indicators. Mineral. Deposita 49, 785–796.
Dare, S.A.S., Barnes, S.-J., Beaudoin, G., 2015. Did the massive magnetite "lava flows" of El Laco (Chile) form by magmatic or hydrothermal processes? New constraints from magnetite composition by LA-ICP-MS. Mineral. Deposita 50, 607–617.
Deckart, K., Bertrand, H., Liégeois, J.-P., 2005. Geochemistry and Sr, Nd, Pb isotopic composition of the Central Atlantic Magmatic Province (CAMP) in Guyana and Guinea. Lithos 82, 289–314.
Dymek, R.F., Owens, B.E., 2001. Petrogenesis of apatite-rich rocks (nelsonites and oxide-apatite gabbronorites) associated with massif Anorthosites. Chem. Geol. 96, 797–815.
Falloon, T.J., Green, D.H., Danyushevsky, L.V., Faul, U.H., 1999. Peridotite Melting at 1.0 and 1.5 GPa: an Experimental Evaluation of Techniques using Diamond Aggregates and Mineral Mixes for Determination of Near-solidus Melts. J. Petrol. 40, 1343–1375.
Frost, B.R., 1991. Introduction to oxygen fugacity and its petrologic importance. Rev. Mineral. Geochem. 25, 1–9.
Frost, B.R., Chamberlain, K.R., Schumacher, J.C., 2000. Sphene (titanite): phase relations and role as a geochronometer. Chem. Geol. 172, 131–148.
Gao, X.Y., Zheng, Y.F., Chen, Y.X., 2011. U-Pb ages and trace elements in metamorphic zircon and titanite from UHP eclogite in the Dabie orogen: constraints on P-T-t path. J. Metamorph. Geol. 29, 721–740.
Garber, J.M., Hacker, B.R., Kylander-Clark, A.R.C., Stearns, M., Seward, G., 2017. Controls on Trace Element Uptake in Metamorphic Titanite: Implications for Petrochronology. J. Petrol. 58, 1031–1057.
Ghiorso, M.S., Evans, B.W., 2008. Thermodynamics of rhombohedral oxide solid solutions and a revision of the FE-TI Two-oxide geothermometer and oxygen-barometer. Am. J. Sci. 308, 957–1039.
Gibson, S.A., Thompson, R.N., Dickin, A.P., Leonardos, O.H., 1996. High-Ti and low-Ti mafic potassic magmas: Key to plume-lithosphere interactions and continental flood-basalt genesis. Earth Planet. Sci. Lett. 136, 149–165.
Gibson, S.A., Thompson, R.N., Dickin, A.P., 2000. Ferropicrites geochemical evidence for Fe rich streaks in upwelling mantle plumes. Earth Planet. Sci. Lett. 174, 355–374.
Griffin, W.L., Powell, W., Pearson, N.J., O'Reilly, S.Y., 2008. GLITTER: data reduction software for laser ablation ICP-MS. Laser Ablation ICP-MS in the Earth Sciences: Current Practices and Outstanding Issues, pp. 308–311.
Gualda, G.A.R., Ghiorso, M.S., 2015. MELTS_Excel: A Microsoft Excel-based MELTS interface for research and teaching of magma properties and evolution. Geochem. Geophys. Geosyst. 16, 315–324.
Gwalani, L.G., Rock, N.M.S., Chang, W.-J., Fernandez, S., Allègre, C.J., Prinzhofer, A., 1993. Alkaline rocks and carbonatites of amba dongar and adjacent areas, Deccan Igneous Province, Gujarat, India: 1. Geol. Petrograph. Petrochem. Mineral. Petrol. 47, 219–253.
Haggerty, S., 1976. Opaque mineral oxides in terrestrial igneous rocks. Oxide Min. 3, 101–301.
Hanski, E.J., Smolkin, V.F., 1995. Iron- and LREE-enriched mantle source for early Proterozoic intraplate magmatism as exemplified by the Pechenga ferropicrites, Kola Peninsula, Russia. Lithos 34, 107–125.
Harlov, D., Tropper, P., Seifert, W., Nijland, T., Förster, H.-J., 2006. Formation of Al-rich titanite ($CaTiSiO_4O$–$CaAlSiO_4OH$) reaction rims on ilmenite in metamorphic rocks as a function of fH_2O and fO_2. Lithos 88, 72–84.
Hayden, L.A., Watson, E.B., Wark, D.A., 2008. A thermobarometer for sphene (titanite). Contrib. Mineral. Petrol. 155, 529–540.
Holm, P.M., Gill, R.C.O., Pedersen, A.K., Larsen, J.G., Hald, N., Nielsen, T.F.D., Thirlwall, M.F., 1993. The Tertiary picrites of West Greenland: contributions from 'Icelandic' and other sources. Earth Planet. Sci. Lett. 115, 227–244.
Holness, M.B., Stripp, G., Humphreys, M.C.S., Veksler, I.V., Nielsen, T.F.D., Tegner, C., 2011. Silicate Liquid Immiscibility within the Crystal Mush: Late-stage Magmatic Microstructures in the Skaergaard Intrusion, East Greenland. J. Petrol. 52, 175–222.
Hunt, J.A., Kerrick, D.M., 1977. The stability of sphene; experimental redetermination and geologic implications. Geochem. Cosmochim. Acta. 41, 279–288.
Hunter, R.H., Sparks, R.S.J., 1987. The differentiation of the Skaergaard intrusion. Contrib. Mineral. Petrol. 95, 451–461.
Jakobsen, J.K., Veksler, I.V., Tegner, C., Brooks, C.K., 2005. Immiscible iron- and silica-rich melts in basalt petrogenesis documented in the Skaergaard intrusion. Geology 33, 885.
Jakobsen, J.K., Veksler, I.V., Tegner, C., Brooks, C.K., 2011. Crystallisation of the Skaergaard Intrusion from an Emulsion of Immiscible Iron- and Silica-rich Liquids: evidence from Melt Inclusions in Plagioclase. J. Petrol. 52, 345–373.
Kohn, M.J., 2017. Titanite Petrochronology. Mineral. Geochem. 83, 419–441.
Kruger, F.J., Cawthorn, R.G., Walsh, K.L., 1987. Strontium isotopic evidence against magma addition in the Upper Zone of the Bushveld complex. Earth Planet. Sci. Lett. 84, 51–58.

Le Bas, M.J., 1981. Carbonatite magmas. Mineral. Mag. 44, 133–140.
Magee, C., Muirhead, J.D., Karvelas, A., Holford, S.P., Jackson, C.A.L., Bastow, I.D., Schofield, N., Stevenson, C.T.E., McLean, C., McCarthy, W., Shtukert, O., 2016. Lateral magma flow in mafic sill complexes. Geosphere 12, 809–841.
Maier, W.D., Barnes, S.J., Groves, D.I., 2012. The Bushveld complex, South Africa: formation of platinum–palladium, chrome- and vanadium-rich layers via hydrodynamic sorting of a mobilized cumulate slurry in a large, relatively slowly cooling, subsiding magma chamber. Mineral. Deposita 48, 1–56.
Marsh, B.D., 1989. Magma Chambers. Annu. Rev. Earth Planet. Sci. 17, 439–472.
Marsh, B.D., 2013. On some fundamentals of igneous petrology. Contrib. Mineral. Petrol. 166, 665–690.
Mucke, A., 2003. Magnetite, ilmenite and ulvite in rocksand ore deposits: petrography, microprobeanalyses and genetic implications. Mineral. Petrol. 77, 215–234.
Namur, O., Charlier, B., Toplis, M.J., Higgins, M.D., Liegeois, J.P., Vander Auwera, J., 2010. Crystallization Sequence and Magma Chamber Processes in the Ferrobasaltic Sept Iles Layered Intrusion, Canada. J. Petrol. 51, 1203–1236.
Namur, O., Charlier, B., Holness, M.B., 2012. Dual origin of Fe–Ti–P gabbros by immiscibility and fractional crystallization of evolved tholeiitic basalts in the Sept Iles layered intrusion. Lithos 154, 100–114.
Namur, O., Abily, B., Boudreau, A.E., Blanchette, F., Bush, J.W.M., Ceuleneer, G., Charlier, B., Donaldson, C.H., Duchesne, J.-C., Higgins, M.D., Morata, D., Nielsen, T.F.D., O'Driscoll, B., Pang, K.N., Peacock, T., Spandler, C.J., Toramaru, A., Veksler, I.V., 2015. Igneous layering in basaltic magma chambers. In: Charlier, B., Namur, O., Latypov, R., Tegner, C. (Eds.), Layered Intrusions. Springer Netherlands, Dordrecht, pp. 75–152.
Néron, A., 2012. Caractérisation géochimiques des oxydes de Fe-Ti dansun dépôt de Fe-Ti-P associe à la suite anorthositique de Lac SaintJean, Québec, Canada (secteur Lac à Paul) et intégration desdonnées du secteur Lac à La Mine. Université du Québec àChicoutimi.
O'Neill, C., Pownceby, M.I., 1993. Thermodynamic data from redox reactions at high temperatures. I. An experimental and theoretical assessment of the electrochemical method using stabilized zirconia electrolytes, with revised values for the Fe - "FeO", Co- CoO, Ni - NiO and Cu- CuzO oxygen buffers, and new data for the W-WO2 buffer. Contrib. Mineral. Petrol. 114, 296–314.
Owens, B.E., Dymek, R.F., 2001. Petrogenesis of the Labrieville Alkalic Anorthosite Massif, Grenville Province. J. Petrol. 42, 1519–1546.
Peng, P., Bleeker, W., Ernst, R.E., Söderlund, U., McNicoll, V., 2011a. U–Pb baddeleyite ages, distribution and geochemistry of 925Ma mafic dykes and 900Ma sills in the North China craton: evidence for a Neoproterozoic mantle plume. Lithos 127, 210–221.
Peng, P., Zhai, M.-G., Li, Q., Wu, F., Hou, Q., Li, Z., Li, T., Zhang, Y., 2011b. Neoproterozoic (~900Ma) Sariwon sills in North Korea: Geochronology, geochemistry and implications for the evolution of the south-eastern margin of the North China Craton. Gondwana Res. 20, 243–254.
Philpotts, A.R., 1982. Composition of Immiscibility Liquids in Volcanic Rocks. Contrib. Mineral. Petrol. 80, 201–218.
Plank, T., Kelley, K.A., Zimmer, M.M., Hauri, E.H., Wallace, P.J., 2013. Why do mafic arc magmas contain ~4 wt % water on average? Earth Planet. Sci. Lett. 364, 168–179.
Prytulak, J., Elliott, T., 2007. TiO_2 enrichment in ocean island basalts. Earth Planet. Sci. Lett. 263, 388–403.
Rollinson, H.R., 1993. Using Geochemical Data: Evaluation, Presentation, Interpretation. Chapter 4. Geology 58 108pp.
Schmidt, M.W., Connolly, J.A.D., Gunther, D., Bogaerts, M., 2006. Element partitioning: the role of melt structure and composition. Science 312, 1646–1650.
Sisson, T.W., Grove, T.I., 1993. Experimental investigations of the role of H_20 in calc-alkaline differentiation and subduction zone magmatism. Contrib. Mineral. Petrol. 113, 143–166.
Snyder, D., Carmichael, I.S.E., Wiebe, R.A., 1993. Experimental study of liquid evolution in an Fe-rich, layered mafic intrusion: constraints of Fe-Ti oxide precipitation on the T-fO_2 and T-ρ paths of tholeiitic magmas. Contrib. Mineral. Petrol. 113, 73–86.
Sobolev, A.V., Hofmann, A.W., Kuzmin, D.V., Yaxley, G.M., Arndt, N.T., Chung, S.-L., Danyushevsky, L.V., Elliott, T., Frey, F.A., Garcia, M.O., Gurenko, A.A., Kamenetsky, V. S., Kerr, A.C., Krivolutskaya, N.A., Matvienkov, V.V., Nikogosian, I.K., Rocholl, A., Sigurdsson, I.A., Sushchevskaya, N.M., Teklay, M., 2007. The Amount of Recycled Crust in sources of Mantle-Derived Melts. Science 316, 412–417.
Solovova, I.P., Girnis, A.V., Kogarko, L.N., Kononkova, N.N., Stoppa, F., Rosatelli, G., 2005. Compositions of magmas and carbonate–silicate liquid immiscibility in the Vulture alkaline igneous complex, Italy. Lithos 85, 113–128.
Toplis, M.J., Carroll, M.R., 1995. An experimental study of the influence of oxygen fugacity on Fe-Ti oxide stability, phase relations, and mineral–melt equilibria in ferro-basaltic systems. J. Petrol. 36, 1137–1170.
Toplis, M.J., Libourel, G., Carroll, M.R., 1994. The role of phosphorus in crystallisation processes of basalt: an experimental study. Geochim. Cosmochim. Acta 58, 797–810.
Veksler, I.V., Charlier, B., 2015. Silicate Liquid Immiscibility in Layered Intrusions. In: Charlier, B., Namur, O., Latypov, R., Tegner, C. (Eds.), Layered Intrusions. Springer Netherlands, Dordrecht, pp. 229–258.
Veksler, I.V., Dorfman, A.M., Danyushevsky, L.V., Jakobsen, J.K., Dingwell, D.B., 2006. Immiscible silicate liquid partition coefficients: implications for crystal-melt element partitioning and basalt petrogenesis. Contrib. Mineral. Petrol. 152, 685–702.
Veksler, I.V., Dorfman, A.M., Borisov, A.A., Wirth, R., Dingwell, D.B., 2007. Liquid Immiscibility and the Evolution of Basaltic Magma. J. Petrol. 48, 2187–2210.
Villiger, S., Ulmer, P., Muntener, O., 2006. Equilibriumand Fractional Crystallization experiments at 0-7GPa; the effect of pressure on phase relation and liquids composition of Tholeiitic Magmas. J. Petrol. 48, 159–184.
Wang, Q., Yang, D., Xu, W., 2012. Neoproterozoic basic magmatism in the southeast margin of North China Craton: evidence from whole-rock geochemistry, U-Pb and Hf isotopic study of zircons from diabase swarms in the Xuzhou-Huaibei area of China. Sci. China Earth Sci. 55, 1461–1479.
Wones, D.R., 1989. Significance of the assemblage titanite + magnetite + quartz in granitic rocks. Am. Mineral. 74, 744–749.
Xirouchakis, D., Lindsley, D.H., 1998. Equilibria among titanite, hedenbergite, fayalite, quartz, ilmenite, and magnetite: experiments and internally consistent thermodynamic data for titanite. Am. Mineral. 83, 712–725.
Yang, J.H., Sun, J.F., Chen, F., Wilde, S.A., Wu, F.Y., 2007. Sources and Petrogenesis of late Triassic Dolerite Dikes in the Liaodong Peninsula: Implications for Post-collisional Lithosphere Thinning of the Eastern North China Craton. J. Petrol. 48, 1973–1997.
Zhang, S.-H., Zhao, Y., Ye, H., Hu, G.-H., 2016. Early Neoproterozoic emplacement of the diabase sill swarms in the Liaodong Peninsula and pre-magmatic uplift of the southeastern North China Craton. Precambrian Res. 272, 203–225.
Zhou, M.F., Robinson, P.T., Lesher, C.M., Keays, R.R., Zhang, C.J., Malpas, J., 2005. Geochemistry, Petrogenesis and Metallogenesis of the Panzhihua Gabbroic Layered Intrusion and Associated Fe-Ti-V Oxide Deposits, Sichuan Province, SW China. J. Petrol. 46, 2253–2280.
Zimmer, M.M., Plank, T., Hauri, E.H., Yogodzinski, G.M., Stelling, P., Larsen, J., Singer, B., Jicha, B., Mandeville, C., Nye, C.J., 2010. The Role of Water in Generating the Calc-alkaline Trend: New Volatile Data for Aleutian Magmas and a New Tholeiitic Index. J. Petrol. 51, 2411–2444.